



















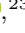







NGDEEP: The Star Formation and Ionization Properties of Galaxies at $1.7 < z < 3.4$

LU SHEN ^{1,2} CASEY PAPOVICH ^{1,2} JASLEEN MATHARU ^{3,4} NOR PIRZKAL ⁵ WEIDA HU ^{1,2}
DANIELLE A. BERG ⁶ MICAELA B. BAGLEY ⁶ BREN E. BACKHAUS ⁷ NIKKO J. CLERI ^{8,9,10}
MARK DICKINSON ¹¹ STEVEN L. FINKELSTEIN ⁶ NIMISH P. HATHI ¹² MARC HUERTAS-COMPANY ^{13,14,15}
TAYLOR A. HUTCHISON ^{16,*} MAURO GIAVALISCO ¹⁷ NORMAN A. GROGIN ¹⁸ ANNE E. JASKOT ¹⁹
INTAE JUNG ²⁰ JEYHAN S. KARTALTEPE ²¹ ANTON M. KOEKEMOER ²² JENNIFER M. LOTZ ²³
PABLO G. PÉREZ-GONZÁLEZ ²⁴ BARRY ROTHBERG ^{25,26} RAYMOND C. SIMONS ²⁷
BRITTANY N. VANDERHOOF ¹² AND L. Y. AARON YUNG ¹²

¹Department of Physics and Astronomy, Texas A&M University, College Station, TX, 77843-4242 USA

²George P. and Cynthia Woods Mitchell Institute for Fundamental Physics and Astronomy, Texas A&M University, College Station, TX, 77843-4242 USA

³Cosmic Dawn Center (DAWN), Denmark

⁴Niels Bohr Institute, University of Copenhagen, Jagtvej 128, DK-2200 Copenhagen N, Denmark

⁵ESA/AURA Space Telescope Science Institute

⁶Department of Astronomy, The University of Texas at Austin, Austin, TX, USA

⁷Department of Physics and Astronomy, University of Kansas, Lawrence, KS 66045, USA

⁸Department of Astronomy and Astrophysics, The Pennsylvania State University, University Park, PA 16802, USA

⁹Institute for Computational and Data Sciences, The Pennsylvania State University, University Park, PA 16802, USA

¹⁰Institute for Gravitation and the Cosmos, The Pennsylvania State University, University Park, PA 16802, USA

¹¹NSF's National Optical-Infrared Astronomy Research Laboratory, 950 N. Cherry Ave., Tucson, AZ 85719, USA

¹²Space Telescope Science Institute, 3700 San Martin Drive, Baltimore, MD 21218, USA

¹³Instituto de Astrofísica de Canarias, La Laguna, Tenerife, Spain

¹⁴Universidad de la Laguna, La Laguna, Tenerife, Spain

¹⁵Université Paris-Cité, LERMA - Observatoire de Paris, PSL, Paris, France

¹⁶Astrophysics Science Division, NASA Goddard Space Flight Center, 8800 Greenbelt Rd, Greenbelt, MD 20771, USA

¹⁷University of Massachusetts Amherst, 710 North Pleasant Street, Amherst, MA 01003-9305, USA

¹⁸Space Telescope Science Institute, Baltimore, MD, USA

¹⁹Department of Physics and Astronomy, Williams College, Williamstown, MA 01267, USA

²⁰Space Telescope Science Institute, Baltimore, MD, 21218, USA

²¹Laboratory for Multiwavelength Astrophysics, School of Physics and Astronomy, Rochester Institute of Technology, 84 Lomb Memorial Drive, Rochester, NY 14623, USA

²²Space Telescope Science Institute, 3700 San Martin Dr., Baltimore, MD 21218, USA

²³Gemini Observatory/NSF's National Optical-Infrared Astronomy Research Laboratory, 950 N. Cherry Ave., Tucson, AZ 85719, USA

²⁴Centro de Astrobiología (CAB), CSIC-INTA, Ctra. de Ajalvir km 4, Torrejón de Ardoz, E-28850, Madrid, Spain

²⁵U.S. Naval Observatory, 3450 Massachusetts Avenue NW, Washington, DC 20392, USA

²⁶Department of Physics and Astronomy, George Mason University, 4400 University Drive, MSN 3F3, Fairfax, VA 22030, USA

²⁷Department of Physics, 196 Auditorium Road, Unit 3046, University of Connecticut, Storrs, CT 06269

ABSTRACT

We use *JWST*/NIRISS slitless spectroscopy from the Next Generation Deep Extragalactic Exploratory Public (NGDEEP) Survey to investigate the physical condition of 178 star-forming galaxies at $1.7 < z < 3.4$. At these redshifts, the deep NGDEEP NIRISS slitless spectroscopy covers the [O II] $\lambda\lambda$ 3726,3729, [O III] $\lambda\lambda$ 4959,5007, H β and H α emission features for galaxies with stellar masses $\log(M_*/M_\odot) \gtrsim 7$, nearly a factor of a hundred lower than previous studies. We focus on the [O II]/[O III] (O₃₂) ratio which is primarily sensitive to the ionization state and with a secondary dependence on the gas-phase metallicity of the interstellar medium. We find significant ($\gtrsim 5\sigma$) correlations

Corresponding author: Lu Shen

lushen@tamu.edu

between the O_{32} ratio and galaxy properties as O_{32} increases with decreasing stellar mass, decreasing star formation rate (SFR), increasing specific SFR ($sSFR \equiv SFR/M_*$), and increasing equivalent width (EW) of $H\alpha$ and $H\beta$. These trends suggest a tight connection between the ionization parameter and these galaxy properties. Galaxies at $z \sim 2 - 3$ exhibit a higher O_{32} than local normal galaxies with the same stellar masses and SFRs, indicating that they have a higher ionization parameter and lower metallicity than local normal galaxies. In addition, we observe a mild evolutionary trend in the O_{32} –EW($H\beta$) relation from $z \sim 0$ to $z \gtrsim 5$, where higher redshift galaxies show increased O_{32} and EW, with possibly higher O_{32} at fixed EW. We argue that both the enhanced recent star formation activity and the higher star formation surface density may contribute to the increase in O_{32} and the ionization parameter.

Keywords: High-redshift galaxies(734); Star formation(1569); Galaxy stellar content(621); Galaxy evolution (594);

1. INTRODUCTION

Star formation is one of the fundamental processes that drive the evolution of galaxies and determine galaxies’ global properties. Globally, the cosmic star formation rate (SFR) density peaked between $z \sim 1$ and 3 (Madau & Dickinson 2014). Understanding the mechanisms behind star formation during this epoch and the factors leading to the subsequent decline is essential for a comprehensive picture of galaxy evolution. This requires investigating the physical conditions of star-forming regions within galaxies, particularly the ionized gas in the interstellar medium (ISM), where recently formed stars are embedded.

The physical properties of ISM are typically characterized by gas-phase metallicity and ionization parameters. Understanding the relationship between these ISM properties and galaxy global properties, such as stellar mass and star formation rate (SFR), offers valuable constraints on the formation and evolution of galaxies (e.g., Somerville & Davé 2015). For example, the evolution of stellar mass and gas-phase metallicity relation has been characterized out to $z \sim 6$ with a clear trend of decreasing metallicity with redshift at fixed stellar mass (Erb et al. 2006; Maiolino et al. 2008; Cullen et al. 2014; Steidel et al. 2014; Sanders et al. 2018, 2021; Curti et al. 2024). The interpretation of these relations and their evolution is that chemical enrichment depends on the galaxy’s star formation history and the interplay between gas infall and outflow.

The ionization parameter (q , or the dimensionless ionization parameter $U \equiv q/c$) is defined as the ratio between the mean hydrogen ionizing photon flux and the density of hydrogen atoms (Dopita & Sutherland 2003; Osterbrock & Ferland 2006). It is typically estimated

from the ratio of emission lines of different ionization stages of the same element, such as the $[O\ III]/[O\ II]$ (O_{32}) ratio (e.g., Kewley & Dopita 2002; Kewley et al. 2019b). The correlation between the O_{32} ratio and the galaxy global properties such as stellar mass, SFR, and specific SFR ($sSFR \equiv SFR/M_*$) has been observed up to $z \sim 3$ (Nakajima & Ouchi 2014; Kewley et al. 2015; Sanders et al. 2016; Kaasinen et al. 2018; Mingozi et al. 2020; Papovich et al. 2022). These studies consistently found that star-forming galaxies (SFGs) at $z \sim 1 - 3$ have significantly higher O_{32} ratios than typical SFGs at $z \sim 0$ by ~ 0.6 dex at a fixed stellar mass. However, the physical cause of the elevated ionization parameter in high-redshift galaxies remains unclear.

It has been suggested that the evolution of the ionization parameter is correlated with the evolving equivalent width (EW) of H recombination lines and $sSFR$ (Kewley et al. 2015; Kaasinen et al. 2018). A high $sSFR$ (or EW) indicates a high ratio of young-to-old stars, which corresponds to a relatively increased flux of hydrogen-ionizing photons from young massive stars. Some other studies have pointed to the increased electron densities (n_e) in high redshift galaxies as a possible factor in increasing the ionization parameter (Davies et al. 2021; Reddy et al. 2023b,a). This is related to the fact that the ionization parameter is determined by hydrogen gas density, which is approximately the electron density (for an ionized gas). In addition, other factors such as low metallicity, a hard ionizing radiation field, and the presence of density-bounded H II regions could increase the O_{32} ratio (Nakajima & Ouchi 2014; Kewley et al. 2019b), which could bias the interpretation of O_{32} and the evolutionary trends of ionization parameter.

To gain a deeper understanding of the physical factors driving the elevated ionization parameter in high-redshift galaxies, we investigate the ionization state of SFGs at $1.7 < z < 3.4$, using the deep, *JWST* NIRISS

* NASA Postdoctoral Fellow

slitless spectroscopy observations from the Next Generation Deep Extragalactic Exploratory Public (NGDEEP) Survey (Bagley et al. 2022; Pirzkal et al. 2023; Shen et al. 2024). The NIRISS data probe observed-frame near-IR wavelengths ranging from 1.0-2.2 μm corresponding to rest-frame 0.37 - 0.81 μm and 0.23 - 0.50 μm for galaxies at $z = 1.7$ and $z = 3.4$, respectively. This data covers strong emission lines ([O II], H β , and [O III]) which trace gas ionization parameters and metallicities for galaxies at $z \sim 1.7 - 3.4$. Importantly, NGDEEP measures these properties for an unbiased galaxy sample with stellar masses of $\log(M_*/M_\odot) \gtrsim 7$ at these redshifts. This enables us to constrain the evolution of ISM properties (i.e., ionization and metallicity) and its correlation to galaxy properties in low-mass galaxies ($M_* < 10^9 M_\odot$). In this paper, we focus on the relationships between the O_{32} ratio and various galaxy properties, comparing them to those measured from local galaxies. We will present results on the evolution with metallicity in a future paper.

The outline for this paper is as follows. In Section 2 we describe the data sets, methods to derive stellar-population properties using broadband data, and sample selection. In Section 3, we present and constrain the relationships between the O_{32} ratio and galaxy properties, including stellar mass, SFR, sSFR, and EW of H α and H β . In Section 4, we discuss the dependence of the O_{32} ratio on the ionization parameter and metallicity, as well as the factors that could influence the ionization parameter. Finally, we summarize our findings in Section 5. Throughout this paper, all magnitudes are presented in the AB system (Oke & Gunn 1983; Fukugita et al. 1996). We adopt a standard Λ -cold dark matter (Λ CDM) cosmology with $H_0 = 70 \text{ km s}^{-1}$, $\Omega_{\Lambda,0} = 0.70$, and $\Omega_{M,0} = 0.30$ (Planck Collaboration et al. 2016).

2. DATA, METHOD, AND SAMPLE SELECTION

2.1. Optical/NIR Imaging and Photometry

We utilized a vast array of deep imaging taken with *HST* and *JWST* available in the HUDF field. This includes *HST* ACS F435W, F606W, F775W, F814W, and F850LP from the latest reductions processed as part of the Cosmic Assembly Near-IR Deep Extragalactic Legacy Survey (CANDELS, Koekemoer et al. 2011; Grogin et al. 2011). We include *JWST* NIR-Cam bands: F090W, F182M, F210M, F277W, F335M, F356W, F430M, F444W, F460M, and F480M from the JADES DR2 (Eisenstein et al. 2023; Rieke & the JADES Collaboration 2023; Williams et al. 2023). The *JWST* NIRISS direct-imaging from NGDEEP is not included in the photometry catalog, because the same filters are

covered by the NIRCam data, which are significantly deeper.

The photometry process is described in detail in Finkelstein et al. (2024). Here we summarize the salient steps. We matched the PSF of all ACS bands and all NIRCam bands bluer than F277W to that of the NIR-Cam F277W image. For bands redder than F277W, we calculated correction factors by convolving the F277W image to the larger PSF, and measuring the flux ratio in the native image to that in the convolved image. We performed photometry using SExtractor (Bertin & Arnouts 1996) in dual image mode, using the inverse-variance-weighted sum of the non-PSF-matched F277W and F356W images as the detection image. We ran the SExtractor in hot and cold modes (Finkelstein et al. *in prep.*). To combine these catalogs, we included all objects in the cold-mode catalog, and we included all objects in the hot-mode catalog whose central pixel did not lie in a cold-mode segmentation map, after that cold-mode segmentation map was dilated by a 5×5 kernel.

We measured flux densities for each galaxy in small Kron apertures. We apply two aperture corrections based on the ratio of the default Kron aperture to our small aperture and an additional aperture correction to measure flux missed on larger scales. We derived uncertainties on the flux densities by placing random non-overlapping apertures with diameters from 0.1-1.5'' in empty regions of the image. We fitted a four-parameter function to the normalized median absolute deviation (NMAD) in each aperture as a function of the aperture area. The flux uncertainty for each object is calculated from this fit for the area in a given object's aperture.

2.2. Grism Data Reduction and Line-flux Measurements

For the analysis of emission-line maps here, we processed the data using the GRIZLI version 1.9.5 (Brammer & Matharu 2021). GRIZLI performs full end-to-end processing of NIRISS imaging and slitless spectroscopic data sets, including retrieving, pre-processing the raw observations for cosmic rays, flat-fielding, sky subtraction, astrometric corrections, alignment, modeling contamination from overlapping spectra, extracting 1D and 2D spectra, and fitting full continuum+emission-line models. For this fitting process, GRIZLI uses a set of templates from the Flexible Stellar Populations Synthesis models (FSPS; Conroy & Gunn 2010) and nebular emission lines. The spectroscopic data is scaled to match the photometry catalog. GRIZLI determines a redshift by minimizing the χ^2 between observed 2D spectra and models. Then it fits emission-line fluxes using the best-fit redshift and accounts for the continua (correct-

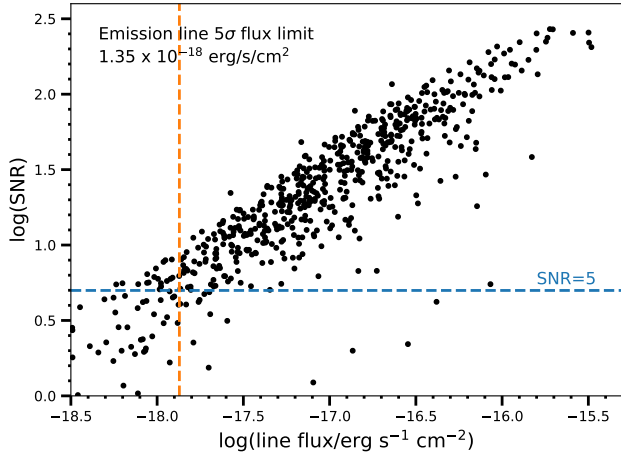


Figure 1. Signal-to-Noise Ratio (SNR) of emission lines as a function of emission line flux for NGDEEP galaxies at $1.7 < z < 3.4$. Emission lines include [O II] $\lambda\lambda$ 3726,3729, H β , [O III] $\lambda\lambda$ 4959,5007, and H α across three filters (F115W, F150W, and F200W).

ing for absorption features, e.g., from Balmer lines) using the best-fit stellar population model. For additional details on GRIZLI and its data products, we refer the reader to Estrada-Carpenter et al. (2019); Simons et al. (2021); Matharu et al. (2021); Papovich et al. (2022); Wang et al. (2022); Simons et al. (2023); Noirot et al. (2023); Matharu et al. (2023).

We adopt the H α , H β , [O II], and [O III] emission line fluxes, equivalent widths, and associated errors measured by GRIZLI. For our selected NGDEEP sample (see Section 2.6), we measure the average emission line 5σ flux limit of 1.35×10^{-18} erg/s/cm 2 as shown in Figure 1. We note that due to the low spectral resolution of the NIRISS grism ($R \sim 150$), the H α and [N II] lines are blended. For the median stellar mass and redshift of the galaxies in our sample, we expect the [N II]/(H α + [N II]) to be ~ 0.05 (Faisst et al. 2018). It is worth noting that the flux measurement method employed by Pirzkal et al. (2023, and Vanderhoof in prep.) adopts more conservative flux uncertainties, which would imply the uncertainties on the line fluxes here are underestimated by a factor of ≈ 1.5 . We therefore adopt the flux uncertainties from GRIZLI for consistency, and we note that if we increased the errors by a factor of 1.5 it would not otherwise impact any of the findings in this paper.

2.3. SED Fitting and Estimating Galaxy Properties

We employed the SED fitting Code Investigating GALaxy Emission (CIGALE) (Boquien et al. 2019; Yang et al. 2020) to estimate properties of the stellar populations of our galaxies using the photometry catalog with flux densities measured in bandpasses spanning the ob-

served wavelength range of $0.43 - 4.8 \mu\text{m}$ (see details in Section 2.1). Note that the NIRISS spectra were not included in the fitting process. However, the redshift was fixed to the value determined from the NIRISS spectra as measured by GRIZLI (see Section 2.2).

Here we described the modules and parameters adopted in CIGALE. We adopted a delayed star formation history (SFH) allowing the τ and stellar age to vary from 0.05–10 Gyr and 0.02–5 Gyr, respectively. In addition to the main star formation history, we allow for a more recent “burst” of star formation. We model this burst as an exponential SFH with a τ allowed to vary from 20 to 100 Myr with an age of 5 and 10 Myr and we allow the mass fraction of this burst (f_{burst}) to vary from 0 to 0.1. We assumed a Chabrier (2003) IMF and the stellar population synthesis models presented by Bruzual & Charlot (2003) with metallicity ranging from Solar (Z_{\odot}) to sub-Solar values ($0.4 Z_{\odot}$ and $0.2 Z_{\odot}$). We include nebular emission using templates of Inoue (2011). We allow the ionization parameter $\log(U)$ to vary between -3 to -1 , the gas metallicity (Z_{gas}) to vary between 0.002 and 0.02, and a fixed electron density of 100 cm^{-3} . The dust attenuation follows the extinction law of Calzetti et al. (2000) for attenuating the stellar continuum and it uses the Cardelli et al. (1989) extinction law with $R_V = 3.1$ for attenuating the emission lines. We allow the dust attenuation in emission lines from nebular regions $E(B - V)_{\text{gas}}$ to vary from 0 to 1.1, and a fixed dust attenuation ratio between emission lines and stellar continuum $E(B - V)_{\text{star}}/E(B - V)_{\text{gas}} = 0.44$. The details of these parameters and values are listed in Table 1.

From CIGALE SED fitting, we adopt the stellar mass (M_*), SFR averaged over 10 Myr as the SED-derived SFR (SFR_{SED}), the color excess of the stellar continuum $E(B - V)_{\text{star}}$, and their associated errors. The sSFR is calculated as $\text{sSFR} \equiv \text{SFR}_{10\text{Myr}}/M_*$. We discuss the different SFR measurements from SED fitting further in Appendix A.

2.4. Dust reddening correction

Ideally, we would use the Balmer decrements (e.g., measured from the H α /H β line ratios) to estimate nebular dust attenuation. However, because not all galaxies have both H β and H α covered or detected by NIRISS, we instead rely on the $E(B - V)$ values derived from SED fitting. Following Sanders et al. (2021), we calibrate a relation between $E(B - V)_{\text{gas}}$ based on the Balmer decrement and continuum reddening $E(B - V)_{\text{star}}$ derived from SED fitting and SFR using 67 SFGs from the NGDEEP survey at $1.7 < z < 2.3$ that has de-

Table 1. Parameters used in the SED fitting with CIGALE.

Parameter	Values
Star formation history (sfhdelayed)	
τ [Myr]	50, 100, 300, 500, 1000, 2000, 3000, 5000, 10000
Age [Myr]	20, 40, 80, 160, 320, 640, 1280, 2000, 3000, 5000
τ_{burst}	20, 50, 100
age_{burst}	5, 10
f_{burst}	0.0, 0.01, 0.05, 0.1
Simple stellar population (Bruzual & Charlot 2003)	
IMF	Chabrier (2003)
Metallicity Z_*	0.004, 0.008, 0.02
Nebular emission (Inoue 2011)	
$\log(U)$	-3, -2.5, -2.0, -1.5, -1
gas metallicity Z_{gas}	0.002, 0.005, 0.011, 0.02
Dust Attenuation (Calzetti et al. 2000)	
$E(B-V)_t$	0, 0.01, 0.05, 0.1, 0.15, 0.2, 0.3, 0.5, 0.7, 0.9, 1.1
$E(B-V)_{factor}$	0.44

tections of both $H\alpha$ and $H\beta$ at $SNR > 5$. These best fits are obtained from a Bayesian linear regression code LINMIX (Kelly 2007), accounting for uncertainties on the two variables. The best-fit parameters are the median of the fitted parameters (the slope and intercept) from 10000 random draws from the posterior, and the associated errors are the average between the 16th and 84th percentiles of each parameter. This LINMIX method is applied throughout the paper to derive fit lines. These relations are:

$$E(B - V)_{gas,calibrated} - E(B - V)_{stars} = (0.332 \pm 0.053) \times \log(SFR_{H\alpha}) + (-0.293 \pm 0.045) \quad (1)$$

$$\log(SFR_{H\alpha}) = (0.879 \pm 0.069) \times \log(SFR_{SED,10Myrs}) + (0.063 \pm 0.060), \quad (2)$$

where $E(B - V)_{gas,calibrated}$ is the calibrated $E(B - V)_{gas}$, $E(B - V)_{stars}$ and $SFR_{SED,10Myrs}$ are derived from CIGALE SED fitting (see Section 2.3), and $SFR_{H\alpha}$ is calculated from the dust-corrected $H\alpha$ luminosity using $E(B - V)_{gas}$ from Balmer decrement and convert to SFR using the Kennicutt & Evans (2012) calibration. This method recovers the Balmer decrement $E(B - V)_{gas}$ with a median offset of 0.04

dex. The calibrated $E(B - V)_{gas}$ and the O_{32} ratio do not vary as a function of stellar mass, though a mild dependence on SFR is observed, with O_{32} potentially being underestimated by 0.04 dex at high SFR ($\log(SFR/M_{\odot} \text{ yr}^{-1}) \sim 1.33$). See more details in Appendix B.

In this paper, for the dust correction of emission lines (i.e., $[O \text{ III}] H\beta$, $[O \text{ II}] H\alpha$), we adopt the calibrated $E(B - V)_{gas}$ calculated from equation 1 and 2, or Balmer decrement $E(B - V)_{gas}$ if $H\alpha$ and $H\beta$ detected with $SNR > 5$. We adopt the Cardelli et al. (1989) extinction model with $R_V = 3.1$. No dust correction is applied for galaxies with $E(B - V) < 0$. The uncertainties in equation 1 and 2 are incorporated into the uncertainties of the dust-corrected emission line fluxes. In detail, for each galaxy, we generate 10000 mock values of emission line fluxes, $E(B - V)_{star}$, SFR, and coefficients in equations 1 and 2 by randomly sampling from Gaussian distributions, with the measured value as the means and associated uncertainties as the standard deviations. For galaxies using Balmer decrement $E(B - V)_{gas}$, we account for the uncertainties in emission line fluxes and $E(B - V)_{gas}$ in the mock sampling process. The uncertainties on dust-corrected emission lines are derived from the 16th and 84th percentiles of the mock distributions. As we discuss in Appendix B, applying different $E(B - V)$ for emission lines (a uniform star-to-gas attenuation ratio of 0.44 or 1) does not affect the significance of relations presented in this paper, nor does it substantially impact the slope. However, the intercepts of these relations would be systematically shifted lower by ~ 0.09 dex or 0.03 dex, respectively. For the dust correction of the continuum, we adopt the $E(B - V)_{star}$ from the SED fits and follow the Calzetti et al. (2000) extinction model with $R_V = 3.1$.

We note that we found a significant fraction (48%) of galaxies having $H\alpha/H\beta$ ratios lower than the intrinsic $H\alpha/H\beta$ value of 2.86 based on the Case B assumption and $T = 10^4$ K and $n_e = 10^2 \text{ cm}^{-3}$. We exclude the possibility that these are caused by low SNR or wavelength-dependent flux calibration. On the other hand, we found significant correlations between the $H\alpha/H\beta$ ratio and stellar mass, SFR, and O_{32} . These correlations suggest that the low $H\alpha/H\beta$ ratios are more likely due to physical conditions, such as a different geometry of dust and gas, and higher temperatures in galaxies with high ionization or low metallicity (Reddy et al. 2015; Scarlata et al. 2024). In such environments, the intrinsic $H\alpha/H\beta$ of galaxies could be lower than 2.86. See more details and discussions in Appendix B.

2.5. The $[O \text{ III}]/[O \text{ II}]$ ratio

Here we focus on the relation between the [O III]/[O II] line ratio and galaxy properties (i.e., stellar mass and star formation). The [O III]/[O II] ratio measures the relative amount of emission from double-ionized oxygen to singly ionized oxygen, which traces the ionization of the gas (e.g., Kewley et al. 2019b). We defined the line ratio O_{32} as:

$$O_{32} \equiv \frac{[\text{O III}] \lambda\lambda 4959, 5007}{[\text{O II}] \lambda\lambda 3726, 3729} \quad (3)$$

where [O III] $\lambda\lambda 4959, 5007$ and [O II] $\lambda\lambda 3726, 3729$ are the sum of the emission from both lines in the doublets (as these are unresolved in the NIRISS spectra) and dust corrected as described in section 2.4. For those with [O II] SNR < 5 , we use the $5 \times$ [O II] flux error as an upper limit on [O II] and, thus, a lower limit on the O_{32} ratio. The uncertainties in O_{32} ratio include the uncertainties on emission line fluxes, $E(B - V)_{\text{star}}$ and uncertainties in converting $E(B - V)_{\text{star}}$ to $E(B - V)_{\text{gas}}$ in equation 1 and 2 (see Section 2.4).

2.6. Sample Selection

Here we use the NGDEEP NIRISS WFSS spectroscopy to study galaxies with [O II] $\lambda\lambda 3726, 3729$ and [O III] $\lambda\lambda 4959, 5007$, with the ratio of these two emission lines tracing the ionization parameter. Our NIRISS F115W+F150W+F200W data cover both lines for galaxies in the redshift range $1.72 < z < 3.44$. Additionally, the data include coverage of $H\beta$ $\lambda 4862$ for all galaxies. For galaxies at $1.72 < z < 2.22$, the data also include coverage of $H\alpha$ $\lambda 6564 + [\text{N II}] \lambda 6548, 6584$.

We selected galaxies from NGDEEP for this study using the following criteria and summarized in Table 2

1. We visually examined all the GRIZLI extractions with F150W AB magnitude < 28.4 , requiring galaxies to have at least one spectral feature detected (i.e., emission line, absorption feature, and D4000 break) and to be well-fitted with GRIZLI. Such spectra were classified as “good”. The F150W magnitude cut was chosen because the fraction of galaxies with good spectra is very low ($< 1\%$) at magnitudes fainter than 28.4. We identified and masked contamination if it affects the emission line region of a galaxy. We then re-ran the GRIZLI fitting, excluding the masked regions. We remove objects if the contamination cannot be masked. Visual examination ensures that the derived redshifts are reliable and that the spectra are not affected by contamination from nearby objects. We identified 471 galaxies through this process.
2. We required the spectroscopic redshift derived from the NIRISS data to lie in the redshift range

of $1.72 < z < 3.44$. This redshift range ensures that [O II] and [O III] are mostly covered by grism. During this step, we also removed any objects where their [O II] or [O III] emission fell too close to the edge of the NIRISS wavelength range. A total of 191 galaxies were identified at this stage.

3. We rejected galaxies identified as AGN by cross-matching to the latest AGN catalog from Lyu et al. (2022) within $1''$. This step removed 9 galaxies identified as AGN.
4. We selected SFGs and quiescent galaxies following the UVJ color-color selection criteria from Whitaker et al. (2011). Four quiescent galaxies are removed in this step. We obtained a total of 178 galaxies following this step. We denote this as the “full sample” and is the main sample in this paper. All of these galaxies have [O III] detections at $> 5\sigma$ in the combined 1D spectra, because the [O III] is the strongest line for the majority of these galaxies, and the redshift identification mostly relies on this emission line. This does open a selection bias (as we require strong lines for selection), and we will further discuss this effect in Section 4.1.
5. Lastly, we require the detection of both [O II] and [O III] emission lines with SNR > 5 in the combined 1D spectra. This produced a sample of 149 galaxies, which we denote as the “final sample”. We also consider and plot those with [O II] SNR < 5 (which we call the “low-SNR sample”), but these galaxies are not included in the calculation of median values or linear relations. Within the final sample, 117 and 75 galaxies have $H\beta$ and $H\alpha$ SNR > 5 , respectively. These samples will be used in Section 3.5.

In the top panel of Figure 2, we show the stellar mass histograms for the full sample, the final sample, and for all “photometric” galaxies in the dataset (including those with photometric redshifts, or spectroscopic redshift if available) in the range of $1.7 < z < 3.4$. The histogram for the photometric galaxy sample is rescaled to match the massive end of that for NGDEEP galaxies. The stellar mass histogram of the full and final samples diverges from that for the photometric galaxies at $\lesssim 10^{8.5} M_{\odot}$. The final sample has a similar histogram as the full sample at the massive end, with a small difference present at lower mass.

The middle panel of Figure 2 shows a probability density function (PDF) of stellar mass for the NGDEEP final sample and also with the galaxies separated by red-

Table 2. Summary of Sample Selection

Sample Selection Criteria	Galaxies
F150W magnitude < 28.4 and quality check	471
$1.72 < z_{\text{spec}} < 3.44$, spectra covers [O II] & [O III]	191
AGN removed	182
full sample: SFGs with UVJ color selection	178
final sample: [O III] & [O II] SNR>5	149
low-SNR sample:	29
[O III] SNR > 5 & [O II] SNR<5	
final sample with H β SNR>5	117
final sample with H α SNR>5	75

NOTE—The names of the samples used throughout this paper are denoted in bold.

shift with $1.7 < z < 2.5$ and $2.5 < z < 3.4$. In the right panel of Figure 2, we show a redshift histogram of the NGDEEP final sample. The median stellar mass and redshift for the final sample are $\log(M_*/M_\odot) = 8.62$ and $z_{\text{med}} = 2.31$, respectively. We divide the final sample into two redshift bins at $1.7 < z < 2.5$ (the $z \sim 2$ bin) and $2.5 < z < 3.4$ (the $z \sim 3$ bin) with 79 and 70 galaxies, respectively. The median stellar mass and redshift are $\log(M_*/M_\odot) = 8.59$ and $z_{\text{med}} = 1.98$ for the $z \sim 2$ bin, and $\log(M_*/M_\odot) = 8.63$ and $z_{\text{med}} = 2.89$ for the $z \sim 3$ bin.

We adopt the peak of stellar mass PDF as the 50% mass completeness by fitting a skew-normal distribution with `scipy skewnorm` package. The 50% mass completeness is $\log(M_*/M_\odot) = 8.50$ for galaxies in the final sample, which is the same when separated in redshift. Therefore, throughout the paper, we adopt $\log(M_*/M_\odot) = 8.50$ as our mass completeness. In particular, we will show all galaxies in our samples in subsequent figures, but we only use galaxies with stellar mass above this limit for fitting linear relations.

2.7. Comparison Galaxy Samples

For comparison, we consider both the nearby samples and galaxies at similar redshifts from the literature. For $z \sim 1 - 2$, we consider two samples: the CANDELS Ly α Emission At Reionization (CLEAR) survey, which measured [O II], [O III], and H β emission features for 196 galaxies at $z \sim 1.1 - 2.3$ using HST WFC3 grisms (Pavovich et al. 2022); and the MOSFIRE Deep Evolution Field (MOSDEF) survey, which obtained spectra for ~ 400 of galaxies at $z \sim 0.8 - 4.4$ using Keck/MOSFIRE (Kriek et al. 2015; Reddy et al. 2015). From CLEAR, we selected 158 galaxies with SNR > 3 for both [O II]

and [O III] emission lines. The median and stellar mass and redshift of CLEAR sample is $\log(M_*/M_\odot) = 9.57$ and $z_{\text{med}} = 1.58$. The dust correction is calculated following the (Calzetti et al. 2000) extinction curve and using the A_V from SED fitting. Stellar mass and SFR are estimated using the SED fitting assuming a Kroupa (2001) IMF. For MOSDEF, we utilized the stacked results from Sanders et al. (2021). Stacking samples were selected from the MOSDEF SFGs, requiring detection of [O III] $\lambda 5007$ with SNR > 3 and spectral coverage of [O II], H β and [O III]. The stacking sample is 280 (155) at $z \sim 2.3$ (3.3) with the median redshift of 2.28 (3.24) and median stellar mass of $\log(M_*/M_\odot) = 9.96$ (9.89). The O₃₂ ratio of MOSDEF stacked spectra is measured with [O III] $\lambda 5007$ /[O II] $\lambda \lambda 3726, 3729$. To match our O₃₂ ratio, we multiply the MOSDEF O₃₂ ratio by $(1 + 1/2.98)$. The dust correction for the MOSDEF stacking results is applied prior to stacking and using the same method as described in Section 2.4).

For $z \sim 0$, we consider four samples: the Sloan Digital Sky Survey (SDSS); the Cosmic Origins Spectrograph Legacy Spectroscopic Survey (CLASSY) treasury (Berg et al. 2022); green pea galaxies (Yang et al. 2017b); and blueberry galaxies (Yang et al. 2017a). The latter two samples are named for their compact and distinctive green and blue colors in SDSS false-color *gri*-band images. The SDSS sample represents the overall $z \sim 0$ population, while the latter three samples are selected to be UV bright (CLASSY) or to have strong emission lines (green peas and blueberry galaxies), which may have properties more similar to those of high redshift galaxies. For the SDSS sample, we adopt emission-line measurements and galaxy properties from the MPA-JHU catalog of measurements for SDSS DR8 (Brinchmann et al. 2004; Kauffmann et al. 2003; Tremonti et al. 2004). We select galaxies with SNR > 3 in all [O II], H β , [O III], and H α emission lines, and selected SFGs based on a BPT diagram (Baldwin et al. 1981). Again, to compare these results to those of our NGDEEP samples, the [O II] flux is obtained by adding [O II] $\lambda 3726$ and [O II] $\lambda 3729$ fluxes, and the [O III] flux is obtained by multiplying [O III] $\lambda 5007$ flux with $(1+1/2.98)$. The dust correction is calculated with H α /H β assuming an intrinsic ratio of 2.86 and following the (Cardelli et al. 1989) extinction curve. We adopted the median estimate of the total stellar mass and SFR PDF as the final stellar mass and SFR. Note that SFRs are derived by combining emission-line measurements and correcting for aperture loss.

For the CLASSY sample, we adopt measurements for all 45 galaxies from (Berg et al. 2022). The O₃₂ ratio of CLASSY sample is measured with [O III] $\lambda 5007$ /[O II] $\lambda \lambda 3726, 3729$. To match our O₃₂ ra-

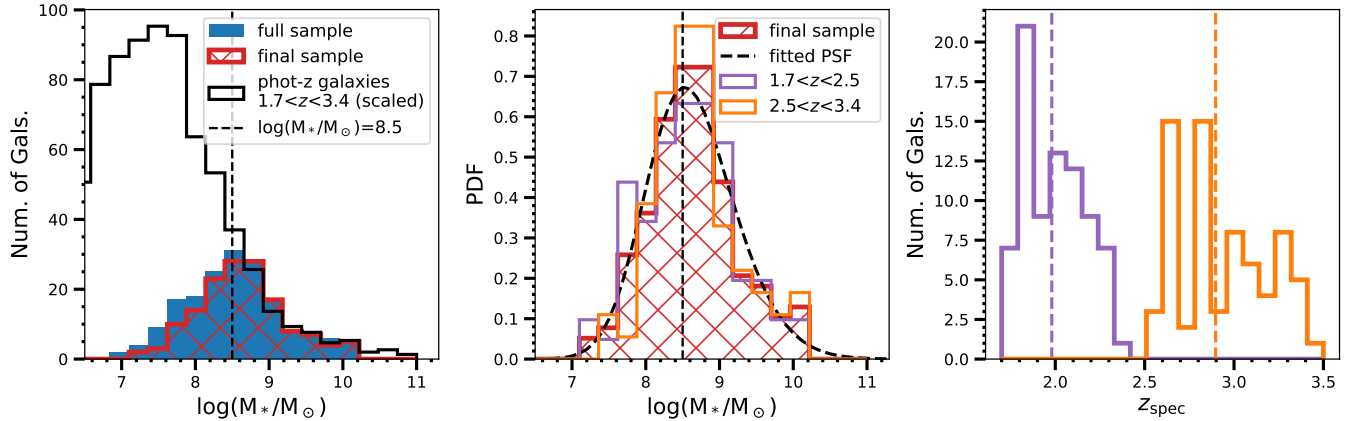


Figure 2. *Left:* The stellar mass histograms for NGDEEP full sample (blue), final sample (red), and “photometric” galaxies (black). The latter includes all galaxies with photometry redshift (spectroscopic redshift if available) at $1.7 < z < 3.4$ (grey). The histogram for the photometric galaxies is rescaled to match the massive end of that for NGDEEP galaxies. *Middle:* The probability density function (PDF) of stellar mass for NGDEEP final sample (red), and the final sample separated by redshift with $1.7 < z < 2.5$ and $2.5 < z < 3.4$ (purple and orange, respectively). The fitted skew normal distribution for the NGDEEP final sample is shown in a black dashed line. In both panels, the vertical dashed line marks the mass completeness of $10^{8.50} M_{\odot}$. *Right:* The redshift histograms of the final sample at $1.7 < z < 2.5$ and $2.5 < z < 3.4$ (purple and orange, respectively). Colored vertical lines indicate the median redshifts.

tio, we multiply the CLASSY O_{32} ratio by $(1+1/2.98)$. For green pea galaxies, we adopted all 43 galaxies with all [O II], $H\beta$, [O III], and $H\alpha$ $SNR > 3$. For blueberry galaxies, we adopted all 36 galaxies with all [O II], $H\beta$, and [O III] $SNR > 3$. No dust correction is applied for blueberry galaxies because the $H\alpha$ fluxes were probably underestimated due to the poor calibration in the red end of spectra (see more in Yang et al. 2017a). SFR is calculated from $H\beta$ for blueberry galaxies and dust-corrected $H\alpha$ for green pea galaxies using the Kennicutt & Evans (2012) calibration.

The SDSS, CLASSY, green pea, and blueberry galaxy catalogs all have [O II] and [O III] measurements, allowing us to compare O_{32} and galaxy properties across samples. However, we note that galaxies’ properties are derived using different SED fitting methods with different wavelength coverage of photometry, which could result in biases during the comparison to our work. In the case of the SFR, our SED-derived SFR values are consistent with $H\alpha$ -derived SFR, where the latter is used to derive SFRs for the SDSS, green pea, and blueberry galaxies. In terms of stellar mass, it is less sensitive to the adopted method and photometry data coverage. In addition, most of these comparison catalogs assumed the same Chabrier (2003) IMF and only CLEAR assumed a Kroupa (2001) IMF. We expect this difference in IMF to have a negligible impact on the derived galaxy properties.

3. RESULTS

In this section, we first compare the SFR – stellar mass distribution of the NGDEEP final sample to the star formation main sequence (SFMS) at similar redshift and to comparison galaxy samples to provide the context of our sample in Section 3.1. Then, we present the relations between the O_{32} ratio and galaxies properties, including stellar mass, SFR, sSFR, and Balmer line EW for our sample, along with comparisons to other galaxy samples in Sections 3.2, 3.3, 3.4 and 3.5, respectively.

3.1. The SFR – Stellar Mass Relationship

The left panel of Figure 3 shows the SED-derived SFRs and stellar masses for galaxies in the NGDEEP final sample and low-SNR sample. The figure also shows the median SFRs and stellar masses of galaxies in the final sample divided into redshift bins of $1.7 < z < 2.5$ and $2.5 \leq z < 3.4$, with the median redshift of $z \sim 2$ and $z \sim 3$, respectively. The median and associated uncertainties are calculated with a bootstrap method to account for uncertainties on individual measurements and the scatter in each bin following Shen et al. (2023). The binning is chosen to have a similar number of galaxies in each bin, with a minimum of 10 galaxies per bin.

We color-code individual galaxies by redshift in the left panel of Figure 3. There is a clear trend with redshift such that SFGs have higher SFR with increasing redshift at fixed stellar mass. This is consistent with the redshift evolution of the SFR- M_{*} relation found by previous studies (e.g., Whitaker et al. 2014; Tomczak et al. 2016).

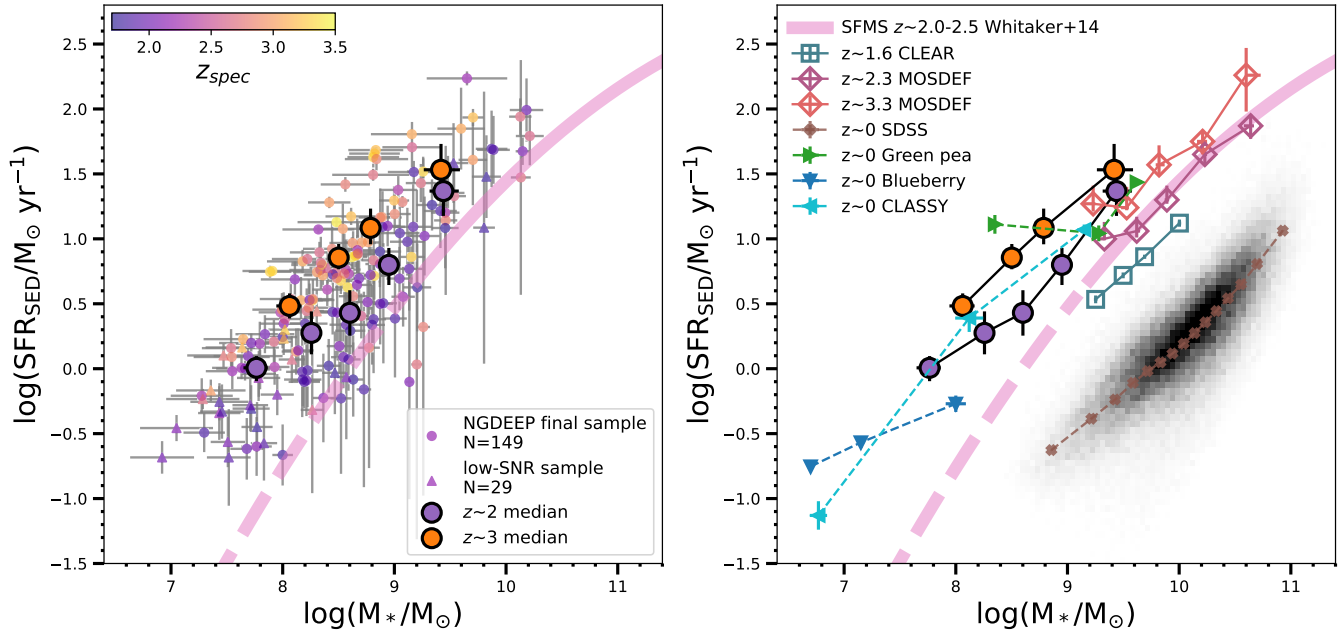


Figure 3. *Left:* The SED-derived SFR versus the stellar mass for galaxies in the NGDEEP final sample (dots) and low-SNR sample (triangle) color-coded by their redshift. The median SFR and stellar mass for galaxies in the final sample at $z \sim 2$ and $z \sim 3$ are shown (in both panels) in black purple- and orange-filled dots, respectively. For comparison, the SFMS for galaxies at $2.0 < z < 2.5$ from Whitaker et al. (2014) is shown down to their mass completeness in the pink line and extended to the lower stellar mass region in the dashed line. *Right:* The median SFR and stellar mass are shown for galaxies at various redshift: $z \sim 1.7$ from CLEAR (Papovich et al. 2022, open blue squares), $z \sim 2.3$ and $z \sim 3.3$ from the MOSDEF stacked sample (Sanders et al. 2021, open magenta and orange diamonds), $z \sim 0$ from SDSS (brown crosses), $z \sim 0$ from CLASSY (Berg et al. 2022, cyan triangles), green pea galaxies at $z \sim 0$ (Yang et al. 2017b, green triangles) and blueberry galaxies at $z \sim 0$ (Yang et al. 2017a, blue triangles). The SDSS sample is shown in the 2D histograms in black. The same median values from the NGDEEP final sample as *left* are shown in black purple- and orange-filled dots. The NGDEEP O₃₂ sample has consistently higher SFR than the SFMS at $z \sim 2 - 2.5$, and has a similar SFR with those of extreme galaxies at $z \sim 0$.

For comparison, we show the star-formation main-sequence (SFMS) derived from a larger sample of SFGs selected from the UVJ color-color method at $2.0 < z < 2.5$ from Whitaker et al. (2014). We compare our galaxies with this SFMS using galaxies having stellar mass above the mass completeness limits of the Whitaker et al. (2014) samples ($\sim 10^{9.2} M_{\odot}$). Our galaxies have a higher SFR than the Whitaker et al. (2014) SFMS with a median difference of $\log(\text{SFR}/\text{SFR}_{\text{MS}}) = 0.33$ dex and a scatter from 0.05 to 0.72 dex from the 16th/84th percentile. This bias is similar to other studies of emission-line selected studies of galaxies (Sanders et al. 2016; Papovich et al. 2022), such that emission-line samples of SFGs tend to have higher SFRs at fixed stellar mass. We will discuss this effect in our results in Section 4.1.

In addition, we find that the median SFR values of galaxies with $M_* < 10^8 M_{\odot}$ at $z < 2.5$ do not decrease with decreasing stellar mass. Instead, galaxies in the low-SNR sample dominate in this low-mass, low-SFR region. Therefore, the flattened median at low mass is mostly likely due to the detection limit, where galaxies

with lower SFR have [O II] (or even [O III]) emission below the detection limit.

The median stellar mass and SFR of local and $z \sim 1-2$ samples are shown in the right panel of Figure 3. The uncertainties on the median are given by $\sigma_{\text{MAD}}/\sqrt{n-1}$, where σ_{MAD} is the median absolute deviation and n is the number of the galaxies in each bin. The CLEAR sample from *HST* grism observations is on average more massive ($10^{9.2}-10^{10} M_{\odot}$) and has lower SFR values than the NGDEEP final sample, due to the lower redshifts of the CLEAR galaxies. The MOSDEF galaxies are also more massive, spanning stellar mass between $10^{9.5}-10^{10.5} M_{\odot}$. The median SFR–mass trend of MOSDEF at $z \sim 2.3$ generally follow the SFMS at $z \sim 2.0 - 2.5$. MOSDEF galaxies at $z \sim 3.3$ have higher SFRs than this SFMS, consistent with the expected evolution of the SFMS. For both redshift samples, the lowest mass bins of MOSDEF galaxies show flattened SFRs, likely due to detection limitations. The SFR–mass relations of the extreme local galaxies from the CLASSY and “green pea” samples are consistent with that of

the NGDEEP final sample, suggesting the properties and physical conditions of these galaxies are comparable with our $z \sim 2-3$ galaxies. On the other hand, the SDSS sample has significantly lower SFR at the same stellar mass compared to galaxies at intermediate redshift and those extreme local galaxies.

3.2. The Mass – O_{32} Relation

Figure 4 shows a tight relationship between the O_{32} ratio and the stellar mass of our final sample, such that the O_{32} ratio decreases as stellar mass increases. We adopt a Spearman rank correlation test to assess the correlation between stellar mass and O_{32} ratio. The test returns a correlation coefficient of -0.73 and a p-value¹ of $\sim 10^{-25}$. This test confirms the significant correlation between O_{32} and stellar mass. The correlation remains significant when separating in redshift.

We measure the median O_{32} in stellar mass bins for galaxies in the final sample and those in two redshift bins at $z \sim 2$ and $z \sim 3$. The difference of mass– O_{32} relation at $z \sim 2$ and $z \sim 3$ is subtle. The median O_{32} at $z \sim 3$ is slightly higher than that at $z \sim 2$ by 17% dex.

We quantify the mass– O_{32} relation with LINMIX using galaxies in the final sample with stellar mass above the mass completeness limit ($> 10^{8.5} M_{\odot}$). The best-fit parameters are reported in Table 3. The median intrinsic scatter measured by LINMIX is 0.05 dex, which accounted for measurement uncertainties. We measure the total scatter of the mass– O_{32} relation by calculating the sum of the squared deviations of data points from the best-fit relation, which represents the spread of the data. The total scatter of the mass– O_{32} relation is 0.24 dex. We show the fit extrapolated to lower stellar mass in Figure 4. The median values follow the fitted line to the stellar mass bin of $\sim 10^8 M_{\odot}$.

In comparison, we show the distribution of O_{32} and stellar mass for the local and $z \sim 1-3$ samples in the right panel of Figure 4. Both the stacked results from MOSDEF at $z \sim 2.3$ and the median from CLEAR at $z \sim 1.6$ are higher than our mass– O_{32} relation by a median of ~ 0.20 dex within the total scatter of our sample. The offset is comparable to the total scatter of our relations, though, a larger offset is seen at the massive end $\log(M_*/M_{\odot}) > 10$. The stacked spectra from MOSDEF at $z \sim 3.3$ are higher than the fitted mass– O_{32} rela-

tion by a median of 0.40 dex. The difference between MOSDEF and our results could be due to differences in selection or detection methods. Our NGDEEP sample extends to fainter magnitudes with $m(\text{F150W}) \leq 28.4$ compared to $m(\text{F160W}) < 25$ mag for MOSDEF (Kriek et al. 2015). This difference is also reflected in the stellar mass range that our NGDEEP sample dominates the lower-mass range ($\log(M_*/M_{\odot}) < 9$) while MOSDEF galaxies are selected with $\log(M_*/M_{\odot}) > 9$. This selection difference could account for the observed offset. Another issue is possibly related to aperture losses. MOSDEF spectra were obtained with a $0.7''$ slit, which could exclude the outer regions of galaxies (Kriek et al. 2015). These outer regions are likely characterized by lower ionization and lower O_{32} ratios, and the aperture corrections may not fully recover the emission line flux from these regions. In contrast, our observations include the full spatial extent of galaxies, potentially leading to an overall lower ionization. Additionally, we cannot rule out the possibility that differences in stellar mass estimates contribute to the discrepancy, as MOSDEF assumes a constant star formation history (Sanders et al. 2021). The comparison between CLEAR and our samples could also be affected by the selection method, as CLEAR extends to $m(\text{F105W}) < 25$ mag and $9.2 < \log(M_*/M_{\odot}) < 10.2$. In addition, the emission line detection limit in CLEAR (3σ of $2 \times 10^{-17} \text{ erg s}^{-1} \text{ cm}^{-2}$) is higher than that of NGDEEP and MOSDEF, it is possible that the CLEAR galaxies with detected [O II] and [O III] are biased toward galaxies with elevated excitation properties compared to typical galaxies at $z \sim 1.5$. Nevertheless, our NGDEEP sample confirms the existence of tight mass– O_{32} relation, consistent with findings at similar redshift, and shows that it extends to lower masses ($\log(M_*/M_{\odot}) \sim 8$).

The mass– O_{32} relation clearly evolved from $z \sim 0$ from SDSS to $z \sim 2$ from NGDEEP, CLEAR, and MOSDEF. The median O_{32} versus M_* values for SDSS show an anti-correlation at low mass ($\sim 10^9 - 10^{10} M_{\odot}$) and flattened at high stellar mass. At fixed stellar mass, galaxies have a higher O_{32} at a higher redshift, and the effect is stronger for galaxies of lower stellar mass. The difference of O_{32} is 0.58 dex at $M_* \sim 10^9 M_{\odot}$. These results suggest that galaxies at $z \sim 1-3$ generally have higher ionization parameters compared to local galaxies at the same stellar mass, assuming the same relation between O_{32} and ionization parameters at both redshifts. In contrast, the O_{32} ratio only slightly increases at a fixed stellar mass from $z \sim 2$ to $z \sim 3$ in NGDEEP and MOSDEF, suggesting a small change in ionization parameter and/or metallicity at fixed stellar mass between these redshifts. At $z \sim 0$, the median O_{32} appears to

¹ The p-value quantifies the probability of obtaining the observed data assuming the null hypothesis (i.e., no correlation) is true. The significance of the correlation by giving the probability that the data are uncorrelated (i.e., the null hypothesis). We reject the null hypothesis if the p-value is ≤ 0.05 , which suggests that the observed correlation is statistically significant.

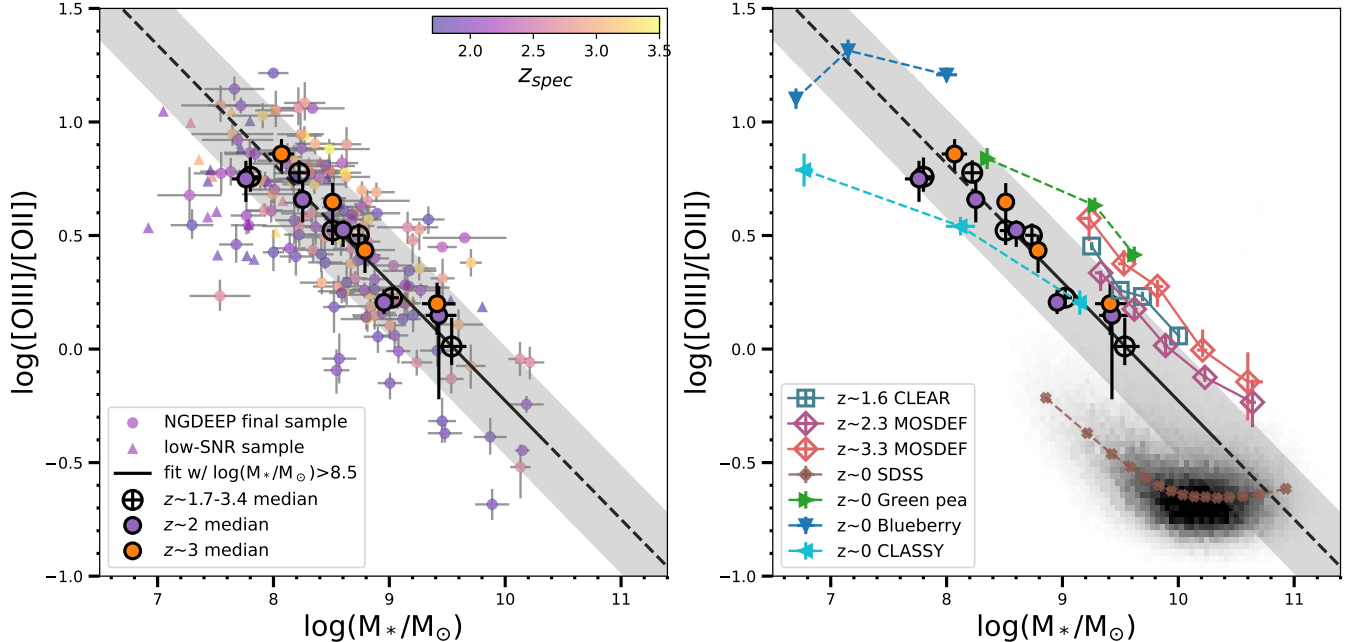


Figure 4. *Left:* The O_{32} ratio versus stellar mass for galaxies in the NGDEEP final sample (dots) and low-SNR sample (triangle), color-coded by redshift. The median O_{32} along the abscissa are shown for galaxies in the final sample (open black circles), for those at $z \sim 2$ and $z \sim 3$ in purple- and orange-filled dots, respectively. The best fit for the NGDEEP final sample with stellar mass $> 10^{8.5} M_{\odot}$ is shown as the solid black lines, and extended to lower stellar mass as the dashed line. The grey region marks the 1σ total scatter. *Right:* The median O_{32} ratios as a function of SFR are shown for CLEAR, MOSDEF, SDSS, CLASSY, green peas, and blueberry galaxies (symbols are the same as in Fig. 3). The SDSS sample is shown in the 2D histograms in black. The same median values and fits from the NGDEEP final sample are shown, identical to those in the *left* panel. The NGDEEP sample shows a tight mass– O_{32} relation.

flatten at high stellar masses $\sim 10^{10} M_{\odot}$. A similar trend is observed in the MOSDEF stacked results. We do not see this flattening in our sample, likely because our sample consists mainly of galaxies in the stellar mass range of $10^8 - 10^{9.2} M_{\odot}$ (16th to 84th percentile), and lacks more massive galaxies.

We then compare to those extreme galaxies at $z \sim 0$. The median O_{32} ratios of CLASSY galaxies align with our mass– O_{32} relation at stellar mass $\gtrsim 10^8 M_{\odot}$. This consistency indicates that these galaxies have similar ISM physical conditions as galaxies at $z \sim 2.5$. At low stellar mass $< 10^8 M_{\odot}$, the median O_{32} ratio of CLASSY galaxies shows lower O_{32} than our extrapolated line. Due to the limited number of galaxies at these lower stellar masses, we cannot draw any definitive conclusions. Green peas have higher O_{32} than our $z \sim 2.5$ relation at the same stellar mass, suggesting that these galaxies have higher ionization parameters and/or lower metallicity than $z \sim 2.5$ galaxies. Blueberry galaxies have similar to higher O_{32} compared to the extended $z \sim 2.5$ relation, but they extend to lower stellar mass regions. Also note that no dust correction is applied for blueberry galaxies, which would slightly lower the

O_{32} though the correction is expected to be minor for galaxies with low stellar mass.

3.3. The SFR – O_{32} Relation

In the left panel of Figure 5, we show the O_{32} ratios as a function of SFR for individual galaxies in the NGDEEP final sample and low-SNR sample. We find a general negative correlation between O_{32} and SFR, where O_{32} decreases as SFR increases. The Spearman correlation test returns a correlation coefficient of -0.41 and a p-value of $\sim 10^{-7}$, confirming the significance of the correlation.

We show the median values of the final sample in two redshift bins at $z \sim 2$ and $z \sim 3$ in the left panel of Figure 5. The median values reveal a clear dependence on the redshift with galaxies at higher redshift having higher O_{32} . The negative correlation between O_{32} and SFR and its redshift evolution is consistent with the redshift-dependent SFR– M_* relation and the tight O_{32} – M_* relation.

We quantify the SFR– O_{32} relation for galaxies in the final sample with $M_* > 10^{8.5} M_{\odot}$ and separated in two redshift bins with LINMIX (Kelly 2007). The best-fit parameters are reported in Table 3. The median intrinsic

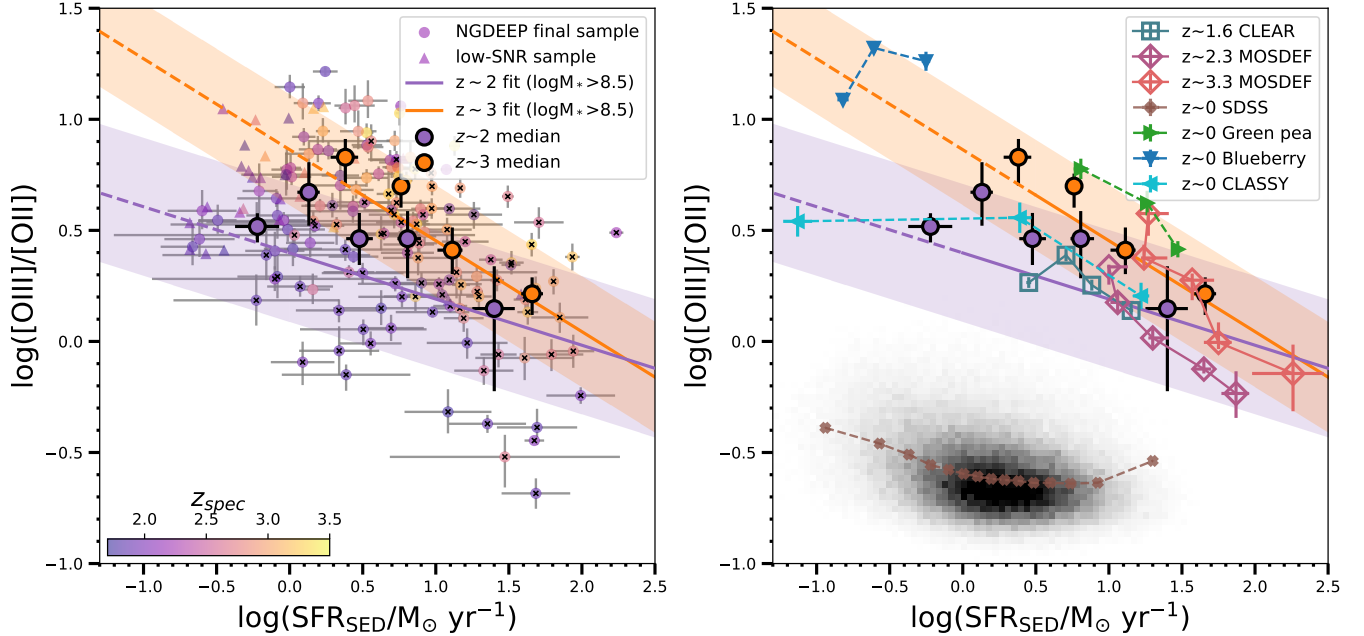


Figure 5. *Left:* The O_{32} versus SFR for galaxies in the NGDEEP final sample (dots) and low-SNR sample (triangle), color-coded by redshift. The median O_{32} values along the abscissa are shown for galaxies at $z \sim 2$ and $z \sim 3$ in purple- and orange-filled dots, respectively. The best fit for galaxies with stellar mass $> 10^{8.5} M_{\odot}$ at $z \sim 2$ and $z \sim 3$ are shown as the solid purple and orange lines, and extended to lower SFR as the dashed line. The color-shaded region marks the 1σ total scatter for each redshift sample. *Right:* The median O_{32} ratios as a function of SFR are shown for CLEAR, MOSDEF, SDSS, CLASSY, green peas, and blueberry galaxies (symbols are the same as in Fig. 3). The SDSS sample is shown in the 2D histograms in black. The same median values and fits from the NGDEEP O_{32} sample are shown, identical to those in the *left* panel. The NGDEEP sample shows a negative SFR– O_{32} relation, with a dependence on redshift.

scatter measured by LINMIX is 0.10 and 0.05 for $z \sim 2$ and $z \sim 3$ fits, respectively. The total scatter of the SFR– O_{32} relations are 0.31 and 0.25 for $z \sim 2$ and $z \sim 3$ fits, respectively. These fits are slightly lower than the median values, particularly at low SFR. This is because the applied mass cut for the fitting excludes some low SFR galaxies, whereas the median values are computed without any mass cut.

We compare our SFR– O_{32} relations to the local and $z \sim 1 - 2$ samples in the right panel of Figure 5. The MOSDEF at $z \sim 2.3$ and CLEAR galaxies are generally consistent with the SFR– O_{32} fit at $z \sim 2$, with an average difference of $\lesssim -0.1$ dex in O_{32} . The MOSDEF at $z \sim 3.3$ is consistent with the SFR– O_{32} fit at $z \sim 3$, with an average difference of ~ 0.02 dex in O_{32} . Similar to the mass– O_{32} relation, the SFR– O_{32} relation evolved from $z \sim 0$ from SDSS to $z \sim 1 - 3$ from NGDEEP, CLEAR, and MOSDEF. At fixed SFR, galaxies have a higher O_{32} at higher redshift, and the effect is stronger for galaxies with lower SFR. The O_{32} difference between SDSS and $z \sim 2$ SFR– O_{32} relation are 1.0 dex and 0.8 dex at $\text{SFR} = 1 M_{\odot} \text{ yr}^{-1}$ and $\text{SFR} = 10 M_{\odot} \text{ yr}^{-1}$, respectively. Compared to those extreme galaxies at $z \sim 0$, the median O_{32} ratios of CLASSY galaxies lie within our

$z \sim 2$ and $z \sim 3$ relations. Green peas and blueberry galaxies on average have higher O_{32} than our $z \sim 3$ and the extended $z \sim 3$ relation, with their median following the upper 1σ total scatter of the $z \sim 3$ relation.

3.4. The sSFR – O_{32} Relation

In the left panel of Figure 6, we show the O_{32} ratios as a function of sSFR for galaxies in the NGDEEP final sample and low-SNR sample. We show the median values for the final sample in two redshift bins. We find a significant positive correlation between the O_{32} ratio and sSFR, with O_{32} increasing as sSFR increases. This is confirmed by a Spearman test with a correlation coefficient of 0.46 and a p-value of $\sim 10^{-9}$. When separating in redshift, the Spearman test returns p-values of $\sim 10^{-10}$ and 0.08 for galaxies at $z \sim 2$ and $z \sim 3$, respectively, suggesting a less significant correlation for $z \sim 3$ galaxies.

We quantify the sSFR– O_{32} relation for the final sample with $M_{*} > 10^{8.5} M_{\odot}$ with LINMIX (Kelly 2007), as reported in Table 3. The median intrinsic scatter measured by LINMIX is 0.06 dex. The total scatter of the sSFR– O_{32} relation is 0.40 dex.

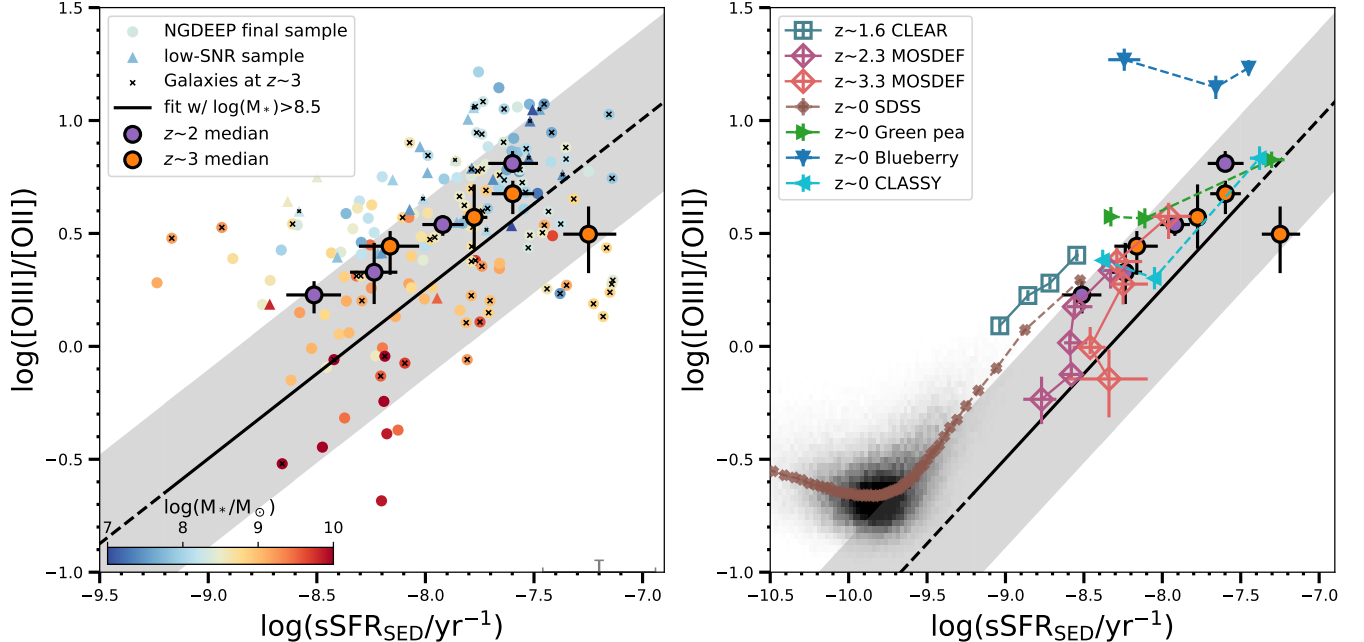


Figure 6. *Left:* The O_{32} versus sSFR for galaxies in the NGDEEP final sample (dots) and low-SNR sample (triangles), color-coded by stellar mass. The median O_{32} values along the abscissa are shown for galaxies at $z \sim 2$ and $z \sim 3$ in purple and orange-filled dots, respectively. The best fit for galaxies with stellar mass $> 10^{8.5} M_{\odot}$ is shown as the solid black lines, and extended to lower/higher sSFR as the dashed line. The grey region marks the 1σ total scatter. *Right:* The median O_{32} ratios as a function of sSFR are shown for CLEAR, MOSDEF, SDSS, CLASSY, green peas, and blueberry galaxies (symbols are the same as in Fig. 3). The SDSS sample is shown in the 2D histograms in black. The same median values and fits from the NGDEEP final sample are shown, identical to those in the *left* panel. Note that the x-axis scale of the right panel is more extended. NGDEEP galaxies show a positive sSFR– O_{32} relation without a redshift-dependence between $z \sim 1.7 - 3.4$, but with a large scatter.

Additionally, we see a diagonal stellar mass gradient as visualized by the color of galaxies with more massive galaxies located in the lower left region, and low-mass galaxies lying in the upper right region. Because of such a mass gradient, the fitted line is consistently lower than the median values across the sSFR range due to the mass cut applied in the fitting.

We compare our sSFR– O_{32} relation to the local and $z \sim 1 - 2$ samples in the right panel of Figure 6. The MOSDEF at $z \sim 2.2$ and $z \sim 3.3$ are generally consistent with the sSFR– O_{32} relation within the 1σ total scatter, with a median difference of ~ 0.2 dex. The CLEAR galaxies are higher than the sSFR– O_{32} relation with a median difference of 0.5 dex. SDSS galaxies dominate in the low sSFR, but have higher O_{32} than the extended of our relation. The median difference between SDSS galaxies and the extended sSFR– O_{32} relation is 1.00 dex and a scatter ranging from 0.65 to 1.41 across the 16th and 84th percentiles.

For those extreme galaxies at $z \sim 0$, the median O_{32} ratios of CLASSY and green pea galaxies are located within 1σ of our relations, with median offsets of 0.16 dex and 0.33 dex, respectively. Blueberry galaxies are

located well above our sSFR– O_{32} relation, with a median offset of 0.71 dex. They exhibit higher O_{32} values compared to our sample at the same sSFR.

3.5. The EW – O_{32} Relation

We study the distribution of O_{32} with $H\beta$ and $H\alpha$ EW. The EW of $H\beta$ and $H\alpha$ provides an independent method for determining the sSFR, as it is a ratio of $H\alpha$ ($H\beta$) flux, both of which are SFR indicators, to the underlying continuum flux, which traces the stellar mass. In Figure 7, we show the O_{32} ratios as a function of $EW(H\beta)$ and $EW(H\alpha)$ for galaxies in the NGDEEP final sample and the low-SNR sample with $H\beta$ and $H\alpha$ SNR > 5 , respectively. We find significant positive correlations between O_{32} and $EW(H\beta)$, and O_{32} and $EW(H\alpha)$. These are confirmed by a Spearman test with a correlation coefficient of 0.71 and 0.63 for the two relations, respectively, and p-values of $\sim 10^{-11}$ and $\sim 10^{-6}$, respectively. We quantify the EW– O_{32} relation for the NGDEEP final sample with $M_* > 10^{8.5} M_{\odot}$ with LINMIX. Best-fitted relations are listed in Table 3.

For the $EW(H\beta)$ – O_{32} relation, we do not find any significant difference in the median values between $z \sim 2$

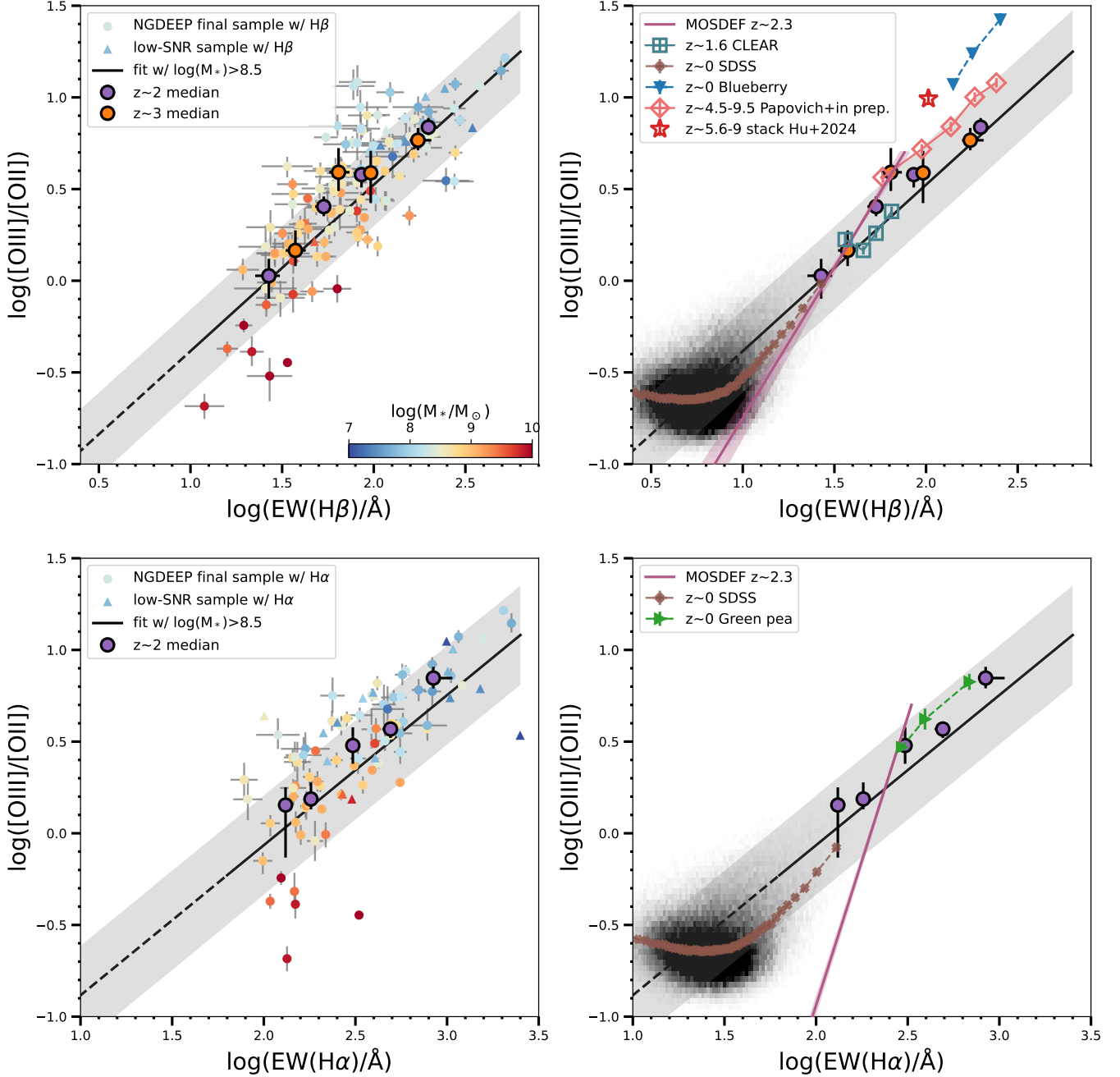


Figure 7. *Lefts:* The relation between the O₃₂ ratio and H β EW (*top*) and H α EW (*bottom*) for galaxies in the NGDEEP final sample and low-SNR sample with H β and H α SNR > 5, respectively. Individual galaxies are color-coded by stellar mass. The median O₃₂ values are shown for galaxies at $1.7 < z < 2.5$ and $2.5 \leq z < 3.4$ as black orange-filled and purple-filled dots, respectively. The best fit for galaxies in the final sample with $M_* > 10^{8.4} M_\odot$ is shown as the solid black line and extended to the low EW region as the dashed black line. *Rights:* Comparison with galaxy samples at different redshift ranges. Median O₃₂ ratios are shown for galaxies at $z \sim 4.5 - 9.5$ from CEERS and JADES (Papovich et al. *in prep.*, open magenta diamonds), galaxies at $z \sim 5.6 - 9$ measured from composite spectra (Hu et al. 2024, red star), CLEAR galaxies at $z \sim 1.1 - 2.3$ (open orange squares), $z \sim 0$ SDSS galaxies (brown crosses), blueberry galaxies (blue triangles), green pea galaxies (green triangles). The SDSS sample is shown in black as the 2D histogram. The relations from Reddy et al. (2018) using MOSDEF galaxies at $z \sim 2.3$ are shown as purple lines. The same median values and fits from the NGDEEP final sample are shown, identical to those in the *left* panel. The NGDEEP sample shows tight EW–O₃₂ relations. A clear evolutionary trend is seen as higher redshift galaxies having higher sSFR and O₃₂.

and $z \sim 3$. Similar to sSFR– O_{32} relation, we see a diagonal stellar mass gradient, where, at a fixed EW (or sSFR), more massive galaxies have lower O_{32} ratios.

In the right panels of Figure 7, we compare our EW– O_{32} relations to the local and $z \sim 1.6$ samples that have available EW measurements. The CLEAR galaxies show an EW($H\beta$)– O_{32} relation consistent with ours, with a small median difference of 0.02 dex. We compared with the EW($H\beta$)– O_{32} and EW($H\alpha$ + $[N\text{ II}]$)– O_{32} relations using MOSDEF galaxies at $z \sim 2.3$ from Reddy et al. (2018). We find that their relations are steeper than our relations, particularly for the EW($H\alpha$). Similarly, the sSFR – O_{32} trends from MOSDEF stacked spectra appear steeper than our median trends. The difference may be due to the different stellar mass ranges in MOSDEF and NGDEEP. The more massive galaxies of NGDEEP ($\log(M_*/M_\odot) \gtrsim 9$) tend to follow the relations from the MOSDEF. However, we find a flatter relation in our sample which includes galaxies at lower masses.

SDSS galaxies mostly occupy the low O_{32} and low EW region, with a tail of high EW and high O_{32} galaxies that tend to align with our $z \sim 2 - 3$ EW– O_{32} relation. We measured a relatively small difference between SDSS and our extended EW– O_{32} relations, with a median difference of 0.01 and -0.06 for the EW($H\beta$) and EW($H\alpha$) relations, respectively. These offset values, both for SDSS and CLEAR, are much smaller than those from sSFR– O_{32} comparison, likely due to the different methods used for stellar mass and SFR measurements, while EW are all calculated in a similar way and account for stellar absorption. Green pea and blueberry galaxies are located above our EW– O_{32} relation, with median offsets of 0.14 dex and 0.48 dex, respectively. However, these samples were selected to be extreme emission-line galaxies, which likely accounts for their offsets.

Furthermore, we compare galaxies at $z \gtrsim 5$ with our EW– O_{32} relation. Firstly, we include 232 galaxies with $[O\text{ II}]$, $[O\text{ III}]$, and $H\beta$ emission line fluxes $\text{SNR} > 3$ measured using the *JWST* NIRSpec PRISM data taken as part of CEERS and JADES surveys (Papovich et al. *in prep.*). The median dust-corrected O_{32} ratios as a function of EW($H\beta$) are shown in the top right panel of Figure 7. Secondly, we include the O_{32} ratio and EW($H\beta$) obtained based on the composite spectrum of 63 galaxies at $5.6 < z < 9$ using the *JWST* medium resolution grating spectra (M-Grating) from CEERS and JADES survey (Hu et al. 2024). Note that this EW($H\beta$) might be underestimated, due to some systematic background issues shown in the composite spectrum (see Figure 2 in Hu et al. 2024 and more discussion there). These $z \gtrsim 5$ galaxies dominate in the high EW $H\beta$ region. The me-

dian O_{32} of $z \gtrsim 5$ galaxies lie slightly above our $z \sim 2 - 3$ relations with a median offset of 0.22 dex. We find an mild evolutionary trend in O_{32} and EW($H\beta$) from $z \sim 0$ to $z \gtrsim 5$ that as higher redshift galaxies have higher EW($H\beta$) and higher O_{32} . These $z \gtrsim 5$ galaxies seem to occupy a region similar to green pea galaxies and blueberry galaxies, suggesting they have similar star formation and ISM properties (i.e., ionization parameter and metallicity). We acknowledge potential biases towards emission line galaxies of these $z \gtrsim 5$ galaxies, which will need future surveys with deeper observations to test. See more discussion in Section 4.1.

4. DISCUSSION

We compared the O_{32} ratio with galaxy properties including stellar mass, SFR, sSFR, and EW of $H\alpha$ and $H\beta$ for NGDEEP galaxies at $z \sim 1.7 - 3.4$ in the final sample (i.e., those galaxies with $[O\text{ II}]$ and $[O\text{ III}] > 5\sigma$ detections). The O_{32} ratio increases with (1) decreasing stellar mass, (2) decreasing SFR, (3) increasing sSFR, and (4) increasing EW of $H\alpha$ and $H\beta$. We quantify the significance and scatter of these relations and summarize them in Table 3. These correlations are qualitatively consistent with results from previous studies at both low and high redshifts (e.g., Nakajima & Ouchi 2014; Kewley et al. 2015; Sanders et al. 2016; Bian et al. 2016; Kaasinen et al. 2018; Kashino et al. 2019; Sanders et al. 2020, 2021; Papovich et al. 2022).

We compare relations from MOSDEF at similar redshift $z \sim 2 - 3$ but derived from more massive galaxies. Galaxies at low mass ($\log(M_*/M_\odot) < 9$) generally follow the same trend as more massive galaxies in the mass– O_{32} relation. However, we find a flattening in SFR–, sSFR– and EW– O_{32} relations at a low SFR, high sSFR, and high EW ($\log(\text{sSFR}/\text{yr}^{-1}) \gtrsim -8$). These regions are dominated by low-mass galaxies ($\log(M_*/M_\odot) < 9$), suggesting a non-linear correlation between O_{32} and galaxies properties. These imply either a non-linear correlation at low masses between ionization (or metallicity) and galaxy properties at low masses or a non-linear correlation between O_{32} and ionization (or metallicity). We further explore this in Section 4.2.

The NGDEEP final-sample galaxies at $z \sim 2 - 3$ have on average higher O_{32} compared to local normal star-forming galaxies from SDSS at the same stellar mass and SFR. This is consistent with other findings for galaxies at $1 \lesssim z \lesssim 3$ (Sanders et al. 2016; Papovich et al. 2022; Sanders et al. 2021). We interpret this as being driven by higher sSFR values in $z \sim 2 - 3$ galaxies, a manifestation of “downsizing”. On the other hand, $z \sim 2 - 3$ galax-

Table 3. Summary of correlations between O_{32} and galaxies properties

Properties	redshift range ^a	c_1^b	c_0^b	intrinsic scatter ^c	total scatter ^d	p-value ^e
M_*	$1.7 < z < 3.4$ ($\langle z \rangle = 2.3$)	-0.52 ± 0.06	4.97 ± 0.59	0.05 ± 0.01	0.24	10^{-25}
SFR	$1.7 < z < 3.4$ ($\langle z \rangle = 2.3$)	-0.21 ± 0.08	0.50 ± 0.09	0.09 ± 0.01	0.30	10^{-7}
SFR	$1.7 < z < 2.5$ ($\langle z \rangle = 2.0$)	-0.21 ± 0.11	0.40 ± 0.11	0.10 ± 0.02	0.31	10^{-3}
SFR	$2.5 < z < 3.4$ ($\langle z \rangle = 2.9$)	-0.41 ± 0.10	0.86 ± 0.14	0.05 ± 0.01	0.25	10^{-10}
sSFR	$1.7 < z < 3.4$ ($\langle z \rangle = 2.3$)	0.74 ± 0.22	6.18 ± 1.76	0.06 ± 0.02	0.47	10^{-9}
EW($H\beta$)	$1.7 < z < 3.4$ ($\langle z \rangle = 2.3$)	0.90 ± 0.11	-1.29 ± 0.20	0.05 ± 0.01	0.23	10^{-11}
EW($H\alpha$)	$1.7 < z < 3.4$ ($\langle z \rangle = 2.3$)	0.82 ± 0.19	-1.69 ± 0.44	0.08 ± 0.02	0.27	10^{-6}

NOTE—^a Only the SFR– O_{32} relation shows a significant redshift dependence, so we separate the SFR– O_{32} relation into two redshift bins. The EW($H\alpha$)– O_{32} relation is restricted to galaxies at $1.7 < z < 2.3$ as our NIRISS data cover $H\alpha$ emission line up to $z = 2.3$.

^b $\log O_{32} = c_0 + c_1 \times x$, where x is the logarithm of the galaxy property in the first column of each row.

^c The median intrinsic scatter is measured from LINMIX, and the uncertainty is derived from the average difference between 16th and 84th percentiles, in a unit of dex.

^d The total scatter is measured by summing the squared deviations between data and the best-fit relation, in a unit of dex.

^e The p-value is measured from the Spearman rank correlation test.

ies have similar to lower O_{32} than those of extreme local galaxies from low-redshift samples such as CLASSY, and the SDSS Green pea, and blueberry galaxies at fixed stellar mass, SFR, sSFR, and EW. Therefore these local samples are more typical of the high- O_{32} tail of the high-redshift samples than of the typical galaxy in the NGDEEP final sample.

Our NGDEEP sample spans a wide range of O_{32} , stellar mass, and sSFR (or EW), extending to lower stellar masses and higher sSFR than previously studied at these redshifts. This helps bridge the gap between the local galaxies and galaxies at $z > 5$. Compared to the higher redshift galaxies, we find an evolutionary trend in EW($H\beta$) – O_{32} from $z \sim 0$ to $z \gtrsim 5$. Higher redshift galaxies have slightly higher O_{32} at fixed EW($H\beta$) (see Figure 7). However, the evolutionary trend in the EW($H\beta$)– O_{32} relation is mild, as the offset in the O_{32} ratios for SDSS and galaxies $z \gtrsim 5$, compared to NGDEEP galaxies, fall within the total scatter of NGDEEP sample. This contrasts with the strong evolution in O_{32} at fixed stellar mass and SFR. This merits future study to understand how this connects to the physical properties of the galaxies as a function of redshift, which we will explore in a future paper.

The mass– O_{32} and EW($H\beta$)– O_{32} relations have the smallest intrinsic and total scatters among properties studies in this paper. On the other hand, the SFR– O_{32} relation has a larger scatter and shows redshift dependence, suggesting that it is more likely a byproduct of the correlation between SFR–mass and mass– O_{32} relations. The O_{32} ratio is sensitive to the ionization

parameter. Papovich et al. (2022) found a tight correlation between O_{32} and ionization parameter derived by modeling the [O II], [O III], and $H\beta$ of the CLEAR galaxies with the MAPPINGS V photoionization models (Sutherland & Dopita 1993; Dopita & Sutherland 1996). They also found a secondary effect that some of the galaxies with high O_{32} ratio shift below the O_{32} –ionization relation, likely due to the effect of metallicity (Strom et al. 2018). This metallicity dependence has been previously seen in photoionization models Kewley et al. (2013), and the existence of anti-correlation between O_{32} and metallicity up to $z \sim 9$ (e.g., Maiolino et al. 2008; Jones et al. 2015; Sanders et al. 2024). Because the O_{32} ratio has a dependence on metallicity, the evolution in the relation between O_{32} and galaxy properties would be a consequence of, or largely driven by, the evolution of the mass–metallicity relation (e.g., (Erb et al. 2006; Maiolino et al. 2008; Zahid et al. 2011, 2014; Sanders et al. 2018; Curti et al. 2020; Sanders et al. 2021)).

In the remainder of this section, we consider potential biases in our results, and we explore the implications of some of the trends further. As mentioned above (Section 2.6), all galaxies in the NGDEEP full sample have [O III] detections above 5σ , which potentially introduces selection bias. We investigate this further and discuss any potential impacts on our results in Section 4.1. We explore the dependence of the O_{32} ratio on ionization parameters and metallicity in Section 4.2. Finally, we discuss the effect on ionization parameters that drives the changes in the O_{32} ratio in Section 4.3.

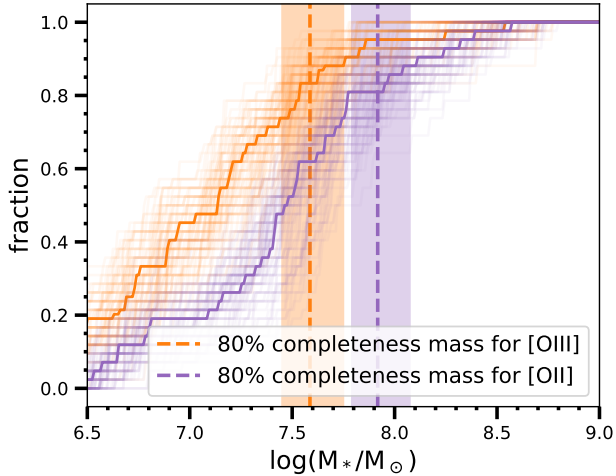


Figure 8. Median fraction of galaxies with [O III] or [O II] detection above our 5σ emission line flux limit from downscaling galaxies as orange and purple solid lines. The fraction distributions of 100 bootstrapping iterations are shown as faint lines. Our empirically derived 80% mass-completeness limits are indicated by vertical dashed lines, and the 16th to 80th percentiles are shown as shaded regions.

4.1. Testing for Selection Bias

During the sample selection (see Section 2.6), we first choose galaxies with reliable redshift from the NIRISS grism data. Because [O III] is the strongest emission line in our sample, we primarily rely on its detection for the redshift determination. However, this approach may introduce a selection bias as it could limit our detection of galaxies with fainter [O III] emission. In addition, our analysis also requires [O II] to be detected, which may lead to missing galaxies with low stellar mass. This is evident in Figure 4, where low-SNR sample (i.e., [O II] $\text{SNR} < 5$) dominated in low mass region. To evaluate the completeness of our sample given the requirement for [O III] or [O II] detection, we adapted and modified the mass-completeness limit method from Tomczak et al. (2014), bootstrapping a completeness limit from the data. We select galaxies that have [O III] (or [O II]) detected $3\times$ above our 5σ emission line flux limit ($1.35 \times 10^{-18} \text{ erg/s/cm}^2$, see Figure 1) and stellar mass $\log(M_*/M_\odot) > 9$ (0.5 dex above the mass completeness limit from Section 2.6). This restricts the sample of galaxies to be sufficient above the detection limits that they should be reasonably complete. We obtain 42 galaxies that meet these criteria, with all of them having [O III] and [O II] above 15σ emission line flux limit. We then randomly select galaxies from this sample with replacement and scale down their masses and emission line fluxes assuming a mass-to-light ratio of 1.54, derived from a fit between stellar mass and F150W flux. From

this scaled-down sample, we then calculate the fraction of galaxies with [O III] ([O II]) above our 5σ emission line flux limit. We then repeat this process by lowering the stellar mass of the selected sample. In this way, we compute the fraction of galaxies recovered as a function of stellar mass. From 100 bootstrapping iterations, we take the median stellar mass that encompasses 80% of the galaxies as the mass-completeness limit. From this technique, we measure an 80% mass-completeness limit of $\log(M_*/M_\odot) = 7.59^{+0.16}_{-0.14}$ for [O III] and $\log(M_*/M_\odot) = 7.91^{+0.16}_{-0.13}$ for [O II]. These limits are lower than the mass completeness derived in Section 2.6 (Figure 2), minimizing the selection bias introduced by the requirement of [O III] and [O II] detection.

With this said, our sample selection also requires that galaxies have rest-frame UVJ colors that classify them as “star-forming” (see Section 2.6 and Table 2). Therefore our sample, by construction, is devoid of quiescent galaxies at these stellar masses and redshifts, which likely contain objects with low or absent nebular emission. Our results therefore apply only to the star-forming population. Our sample is biased to higher SFRs at fixed stellar mass compared to measurements of the SFMS at the same redshifts (see Section 3.1 and Figure 3). This bias is likely related to the fact that our sample is based on emission-line selection, while most measurements of the SFMS used photometric bands with color-selection of star-forming galaxies (e.g., Whitaker et al. 2014; Tomczak et al. 2016). We also note that the SFR values are calculated in different methods that we adopt SFR from SED fitting and well-matched with $H\alpha$ -derived SFR, while, Whitaker et al. (2014) adopted SFR calculated from modeling the broadband imaging from the rest-frame UV to mid/far-IR.

In Section 3.5, we compared our EW- O_{32} relation with those derived from $z \sim 5$ samples. These high redshift samples are from CEERS and JADES spectroscopic samples which could be biased towards emission line galaxies and affected by their pre-selection methods. Nevertheless, we see only mild evolution toward higher O_{32} values at fixed EW from $z \sim 2$ to $z > 4.5$. Any bias would likely act to bring these closer in line. Future studies with deeper spectroscopy, such as Dickinson et al. (2024) will test for bias and better measure this evolution.

4.2. The Dependence of O_{32} on Ionization Parameter and Metallicity

To investigate the O_{32} ratio dependence on ionization parameter and metallicity, we applied the Python version of code “Inferring the gas-phase metallicity (Z) and Ionization parameter” (IZI, Blanc et al. 2015) de-

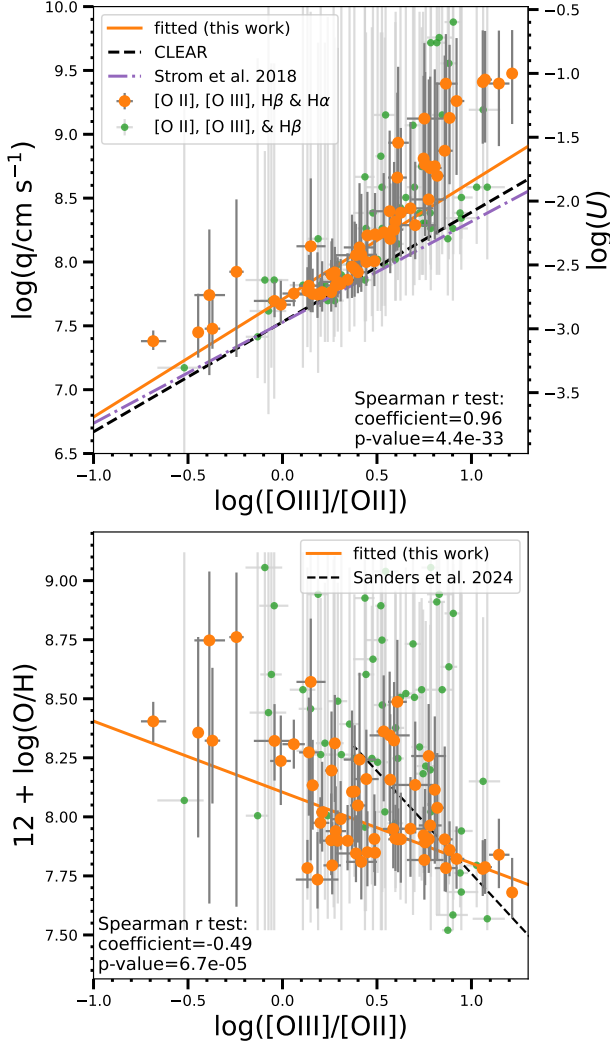


Figure 9. The distribution of ionization parameter (q , *top*) and metallicity ($12 + \log(O/H)$, *bottom*) as function of O_{32} . Galaxies with all four emission lines $> 5\sigma$ and with three lines ($[O\ II]$, $[O\ III]$, and $H\beta$) $> 5\sigma$ are shown in orange and green, respectively. The orange solid lines show a linear fit to the NGDEEP galaxies with all four emission line detection. The *top* panel shows the relations from CLEAR galaxies (Papovich et al. 2022) (black dashed line) and a sample of $z \sim 2.3$ SFGs from Strom et al. (2018) (purple dashed line). The *bottom* panel shows the relation derived from a sample of $z \sim 2-9$ galaxies from Sanders et al. (2024) (black dashed line). While O_{32} correlates with both the ionization parameter and metallicity, the relationship between O_{32} and the ionization parameter is more pronounced.

veloped by Mingozi et al. (2020) to our dataset. IZI is a Bayesian code that computes posterior likelihoods for the gas-phase metallicity and the ionization parameter by comparing the measured emission line fluxes to predictions from the photoionization models. Based on the original IZI, the new Python version adds the op-

tion of using a more efficient Markov-chain Monte-Carlo (MCMC) algorithm and simultaneously fits the dust attenuation following the Calzetti et al. (2000) extinction law. However, the dust-attenuation modeling requires coverage of both $H\beta$ and $H\alpha$, while $[O\ II]$, $[O\ III]$, and $H\beta$ are the minimum needed to constrain metallicity and the ionization parameter. For the 60 galaxies in the NGDEEP final sample with all four emission lines ($[O\ II]$, $[O\ III]$, $H\beta$, and $H\alpha + [N\ II]$) detected with $SNR > 5$, we use the MCMC algorithm. For the 57 galaxies in the NGDEEP final sample only with $[O\ II]$, $[O\ III]$, and $H\beta$ $SNR > 5$, we use the original IZI algorithm and the dust-corrected fluxes following Section 2.4.

For the photoionization models, we adopt the MAPPING V grid models (Kewley et al. 2019b,a). We generated isobaric models with the ISM pressure of $\log(P/k)[K\ \text{cm}^{-3}] = 7$, a grid of ionization parameters $\log(q)$ [cm s^{-1}] from 6 to 10 in intervals of 0.25 (corresponding to $\log(U)$ from -4.5 to -0.5), and a grid of metallicities (Z) with $[0.05, 0.2, 0.4, 1.0] Z_{\odot}$ (Jung et al. 2024). The choice of ISM pressure is motivated by the combination of median electron density, $n_e \sim 250 - 300\ \text{cm}^{-3}$ for galaxies at $z \sim 2-3$ (Sanders et al. 2016; Strom et al. 2017) and the nebular temperature of $\sim 10,000-20,000\text{K}$ (Sanders et al. 2020). We also tested models with $\log(P/k) = 6.5$ and $\log(P/k) = 7.5$. Adopting these models does not alter our conclusions.

We show the ionization parameter as a function of O_{32} for our NGDEEP final sample in the top panel of Figure 9. The ionization parameter increases as O_{32} increases. The Spearman correlation test returns a correlation coefficient of 0.96 and a p-value of $\sim 10^{-33}$ with all four emission lines, and a p-value of $\sim 10^{-42}$ when including galaxies with three emission lines. We fit a linear relation between $\log(O_{32})$ and $\log(q)$ for galaxies with all four emission lines using LINMIX:

$$\log q = (7.71 \pm 0.04) + (0.91 \pm 0.10) \times \log(O_{32}) \quad (4)$$

where the ionization parameter, q , is in the units of cm s^{-1} . The total scatter of the $O_{32}-q$ relation is 0.32 dex.

The large scatter is primarily driven by high O_{32} ($\log(O_{32}) > 0.8$ or $\log(q) > 8.5$), where galaxies have higher $\log(q)$ values than predicted by the linear fit. It is known that $\log(O_{32})$ versus $\log(q)$ is sub-linear at the high O_{32} where the slope of $\log(O_{32})-\log(q)$ relation decreases at high q (Kewley & Dopita 2002; Sanders et al. 2016), or in the $\log(q)-\log(O_{32})$ plot (as shown in Figure 9), the slope increases at high O_{32} . Meanwhile, it is interesting that among galaxies with all four emission lines detected, 10 galaxies with $\log(O_{32}) > 0.8$, 8 of them have no dust attenuation with $E(B - V)_{\text{gas}} = 0$,

and the remaining 2 have low dust attenuation with $E(B - V)_{\text{gas}} \sim 0.09$. These galaxies also appear to have low metallicity, as shown in the bottom panel of Figure 9. The high ionization and low metallicity of these galaxies suggest that they may have a high electron temperature in these galaxies (e.g., Yates et al. 2020). Because the intrinsic ratio of Balmer decrement is temperature dependent, with 2.86 for 10^4 K and decreasing to 2.79 for 1.5×10^4 K, a lower intrinsic ratio would be appropriate for these galaxies. However, in IZI (and as adopted in this paper), the intrinsic ratio of $H\alpha/H\beta$ is assumed to be 2.86. This assumption may force IZI to increase the ionization parameter to model the emission line ratios to account for the low $E(B - V)$ in these galaxies. We show the 1D spectra of two examples of these galaxies and their PDFs from IZI in Figure 10.

This linear fit is slightly steeper than those obtained from other studies at these redshifts (Strom et al. 2018; Papovich et al. 2022). This difference mostly appears in the high O_{32} region, where the majority of galaxies from Papovich et al. (2022) and Strom et al. (2018) do not extend to these high O_{32} ratios. Therefore, our results suggest the linear relation between O_{32} and the ionization parameter breaks down at high values of this ratio ($\log(O_{32}) > 0.8$).

We show the metallicity as a function of the O_{32} ratio for our NGDEEP final sample in the bottom panel of Figure 9. The metallicity decreases with O_{32} increases. The Spearman correlation test returns a correlation coefficient of -0.49 and a p-value of $\sim 10^{-5}$ with all four emission lines and a p-value of $\sim 10^{-4}$ when including galaxies with three emission lines.

We quantified the (anti-)correlation between $\log(O_{32})$ and $12 + \log(O/H)$ using galaxies with all four emission lines ($[O \text{ II}]$, $[O \text{ III}]$, $H\beta$, and $H\alpha + [N \text{ II}]$) using LINMIX:

$$12 + \log(O/H) = (8.10 \pm 0.04) + (-0.30 \pm 0.06) \times \log(O_{32}), \quad (5)$$

where the 1σ total scatter is 0.22 dex. Our fitted linear relation is flatter than that from Sanders et al. (2024), who derived their relation using metallicity from the direct T_e method from a sample of galaxies at $z \sim 2 - 9$. However, our data points are scattered around their fit at high O_{32} region or low metallicity regions. Our sample extends to low O_{32} region where Sanders et al. (2024) did not cover, while this region predominantly drives our fit. Overall, our results suggest that the O_{32} ratio is a strong tracer of gas ionization parameter, with a secondary dependence on metallicity.

The tight mass- O_{32} relation with a scatter of 0.24 dex is difficult to explain by the scatter of O_{32} -metallicity calibrations (~ 0.29 dex from Sanders et al. 2024 and 0.22 dex from our data) and the scatter of mass-

metallicity relation (~ 0.14 dex from Sanders et al. 2021). This scatter is also revealed from the distribution of O_{32} and $R_{23} \equiv ([O \text{ III}] + [O \text{ II}]/H\beta)$ which is sensitive to the gas-phase metallicity (Nakajima & Ouchi 2014; Sanders et al. 2016; Papovich et al. 2022). Although, we cannot rule out the possible effect of the metallicity on the mass-, SFR- and sSFR- O_{32} relations, the ionization parameter may play a more important role in these O_{32} - galaxy properties relations.

4.3. The Relation between the $[O \text{ III}]/[O \text{ II}]$ Ratio, Ionization Production, and SFR

As the O_{32} ratio primarily depends on the ionization parameter, in this section, we focus on the possible effect on the ionization parameter that drives the changes in the O_{32} ratio. The ionization parameter is, by definition, the ratio of the hydrogen ionizing photon flux and the density of hydrogen atoms. For a radiation-bounded nebula, the average ionization parameter can be written as:

$$q = \left(\frac{3Qn_H\epsilon\alpha_B^2}{4\pi} \right)^{1/3} \quad (6)$$

where Q is the ionizing photon production rate, α_B is the case-B hydrogen recombination coefficient, n_H is the number density of hydrogen, and ϵ is the volume filling factor of the gas. Here, we assume no change in α_B and ϵ for galaxies with different SFR and M_* and across redshift (see more discussion in Papovich et al. 2022). Thus, the ionization parameter in this case depends only on Q and n_H .

4.3.1. Ionizing photon production rate

The ionizing photon production rate depends on the properties of massive stars, their evolution, and the IMF. We estimate the ionizing photon production rate Q following Leitherer & Heckman (1995) and assuming an ionizing photon escape fraction of zero:

$$Q = 7.35 \times 10^{11} L(H\alpha) \text{ [s}^{-1}\text{]} \quad (7)$$

where the $L(H\alpha)$ is the dust-corrected $H\alpha$ luminosity in units of erg s^{-1} . $L(H\beta)$ is converted to $L(H\alpha)$ assuming the intrinsic ratio of $H\alpha/H\beta = 2.86$ (as we discussed in Section 4.2, this may not be valid for all galaxies in our sample). We also adopt the ionizing production efficiency ξ_{ion} defined as the ionizing photon production rate per unit UV luminosity, as follows:

$$\xi_{ion} = \frac{Q}{L(UV)} \text{ [s}^{-1}\text{/erg s}^{-1} \text{ Hz}^{-1}\text{]} \quad (8)$$

where $L(UV)$ is the intrinsic UV luminosity at rest-frame 1500 Å. We adopt the rest-frame FUV luminosity from CIGALE SED fits for each galaxy in our sample and

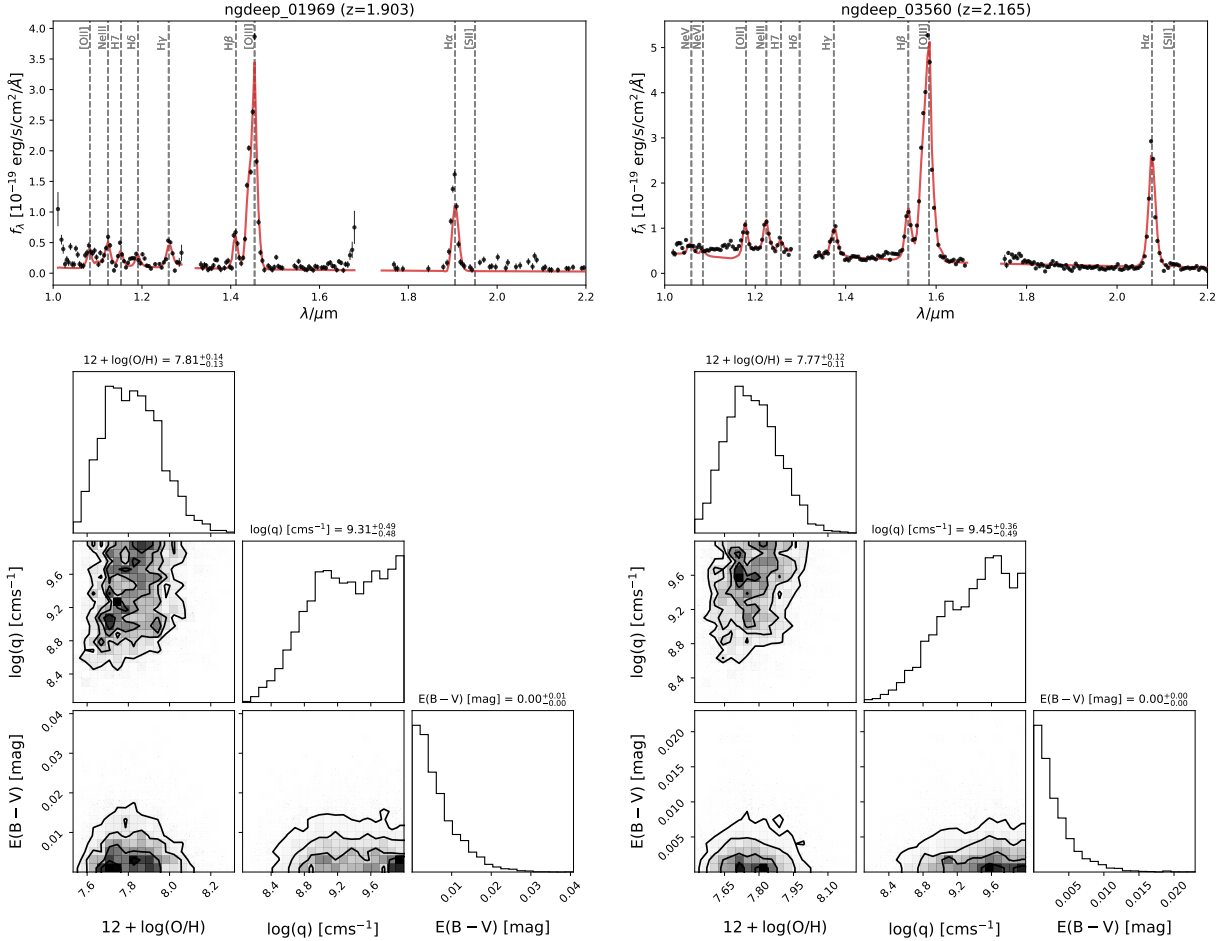


Figure 10. *Top:* 1D spectrum of two galaxies with $\log(\text{O}_{32}) > 0.75$ and $|\text{ZI}|$ -derived $E(B-V) \simeq 0$. Each panel shows the NIRISS grism data (black dots) along with the best-fit spectrum (red line). Important emission lines are marked by vertical grey dashed lines. *Bottom:* The corner plot of $12 + \log(\text{O}/\text{H})$, $\log(q)$, and $E(B-V)$ from $|\text{ZI}|$ for the same galaxies as *top* panel. The median and associated uncertainties are displayed on the top of the histograms.

convert it to intrinsic UV luminosity by correcting the dust with $E(B-V)_{\text{star}}$ from SED fitting and following the Calzetti et al. (2000) law (see more details in Section 2.4).

In the top panel of Figure 11, we show the distribution of the Q and ξ_{ion} values as a function of O_{32} for the NGDEEP final sample with $\text{H}\alpha$ or $\text{H}\beta$ $\text{SNR} > 5$ detection. For galaxies with both $\text{H}\alpha$ and $\text{H}\beta$ detections, we used values from $\text{H}\alpha$, which typically has higher SNR. Additionally, the $\text{H}\alpha$ and $\text{H}\beta$ derived values are consistent for these galaxies, as demonstrated by $\text{H}\alpha$ - and $\text{H}\beta$ - derived SFR in Figure A1. We find a negative correlation between O_{32} and Q with a Spearman rank correlation coefficient of -0.29 and a p-value of 0.001 when including galaxies with $\text{H}\alpha$ or $\text{H}\beta$. The significance of this correlation decreases, with the p-value reduced to 0.04 , when only including galaxies with $\text{H}\alpha$ detections. Because Q depends only on $\text{H}\alpha$ and $\text{H}\beta$ luminosity, which traces the SFR (also see Figure A1),

Q versus O_{32} is similar to the SFR versus O_{32} as shown in Figure 5. However, as discussed in Section 4, the SFR- O_{32} is largely a byproduct of the mass- O_{32} and SFR-mass relations. This mostly rules out the possibility that the ionizing photon production rate plays a dominant role in driving the O_{32} ratio. We compare results from Reddy et al. (2023a), who studied a sample of 48 SFGs at $z = 2.7 - 6.3$ with O_{32} spanning a range of $0.5 - 100$. They found no correlation between the ionizing photon production rate between low- and high- O_{32} galaxies with mean O_{32} values of 1.98 and 6.06 , respectively, as shown in Figure 11. Their mean Q values are higher than the trend derived from our sample at fixed O_{32} , which could be due to their sample containing galaxies at higher redshift.

In the bottom panel of Figure 11, we find a mild positive correlation between O_{32} and ξ_{ion} such that ξ_{ion} increases with increasing O_{32} . The Spearman rank correlation test confirms the significance of this relation,

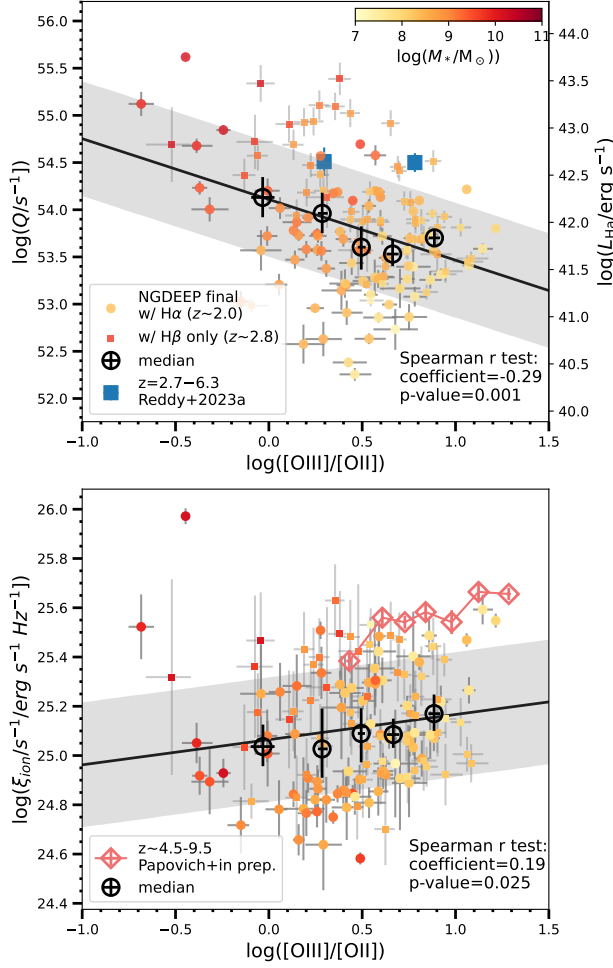


Figure 11. The distribution of O_{32} and ionizing photon production rate Q (top) and ionizing production efficiency ξ_{ion} (bottom) for the NGDEEP final sample with $H\alpha$ or $H\beta$ SNR > 5 detections, color-coded by stellar mass. The median values and best fits for the NGDEEP O_{32} galaxies with $H\alpha$ or $H\beta$ detection (without mass cut) are shown as black dots and solid black lines, and 1σ total scatter is shown as the grey regions. Results from the Spearman rank test are shown as well. The median values of galaxies at $z = 2.7 - 6.3$ from Reddy et al. (2023a) are shown as blue squares in the top panel. The median values of galaxies at $z \sim 4.5 - 9.5$ from CEERS and JADES (Papovich et al. *in prep.*) are shown in open magenta diamonds. Both Q and ξ_{ion} show correlations with O_{32} .

with a correlation coefficient of 0.19 and a p-value of 0.03 when considering galaxies with $H\alpha$ or $H\beta$ detection. The p-value decreases to 0.003 when only galaxies with $H\alpha$ detection are included. The scatter is also non-negligible, 0.26 dex. This could be related to the star formation history of galaxies. The ξ_{ion} values are calculated using the $H\alpha/UV$ ratio, which is commonly used as a tracer for recent bursty star-formation activity (e.g.,

Emami et al. 2019; Guo et al. 2016; Faisst et al. 2019). An elevated $H\alpha$ emission with respect to the UV continuum is a sign of bursty star-formation activity in the past ~ 10 Myr. Similarly, the $EW(H\alpha)$ and sSFR are sensitive to recent star-formation activity. The difference between $EW H\alpha$ and $H\alpha/UV$ ratio is their denominator: the stellar continuum flux and UV continuum flux, respectively. The UV continuum flux traces SF activity in the recent 100-200 Myr. Thus, the two measurements are comparable for a galaxy with an age less than ~ 100 -200 Myr or a galaxy with a constant star formation history. Therefore, it is not surprising that a correlation between ξ_{ion} and sSFR exists for high redshift galaxies up to $z \sim 7$ (Faisst et al. 2019; Emami et al. 2020; Endsley et al. 2021; Emami et al. 2020; Prieto-Lyon et al. 2023) and for extreme galaxies at lower redshift $z \sim 1$ (Tang et al. 2019; Izotov et al. 2021). In Section 3.4, we found O_{32} is correlated with sSFR and $EW H\alpha$. Here we find that O_{32} is correlated with ionizing production efficiency, confirming the connection between ionization parameters and recent star-formation activity.

In addition, we compare galaxies at $z \sim 4.5 - 9.5$ from Papovich et al. (*in prep.*) with our $O_{32}-\xi_{ion}$ relation. The median ξ_{ion} of $z > 5$ galaxies generally follows our relation but is offset to slightly higher ξ_{ion} at fixed O_{32} . The higher ξ_{ion} could be due to a recent starburst which increases the number of massive young stars and boosts the production of ionizing photons. This is consistent with the comparison of $EW(H\beta)-O_{32}$ relation where the $z > 5$ galaxies tend to have higher $EW(H\beta)$ than our NGDEEP galaxies at $z \sim 2 - 3$ (see Figure 7). It is unclear what causes the shift toward higher ξ_{ion} with increasing redshift, though we expect it could be due to low metallicity as metal-poor stars are hotter and more efficient at generating ionizing radiation.

One galaxy (NGDEEP_02938) is significantly offset from the fitted relation, with very high ionizing production efficiency, ξ_{ion} , and relatively low O_{32} ratio. We conclude this offset is likely linked to the fact that it has the highest $E(B - V)$ in our sample, with $E(B - V) = 1.13$ from Balmer decrement and $E(B - V)_{star} = 0.48$ from SED fitting. These values correspond to an attenuation of $A_V \gtrsim 1.5$, and an optical depth of $\tau \gtrsim 1.6$, indicating the galaxy is optically thick. Due to the optical thickness, the UV luminosity of this galaxy could be underestimated as the intrinsic UV emission may be higher than what is observed. This underestimation could lead to an overestimation of the ξ_{ion} .

4.3.2. SFR surface density

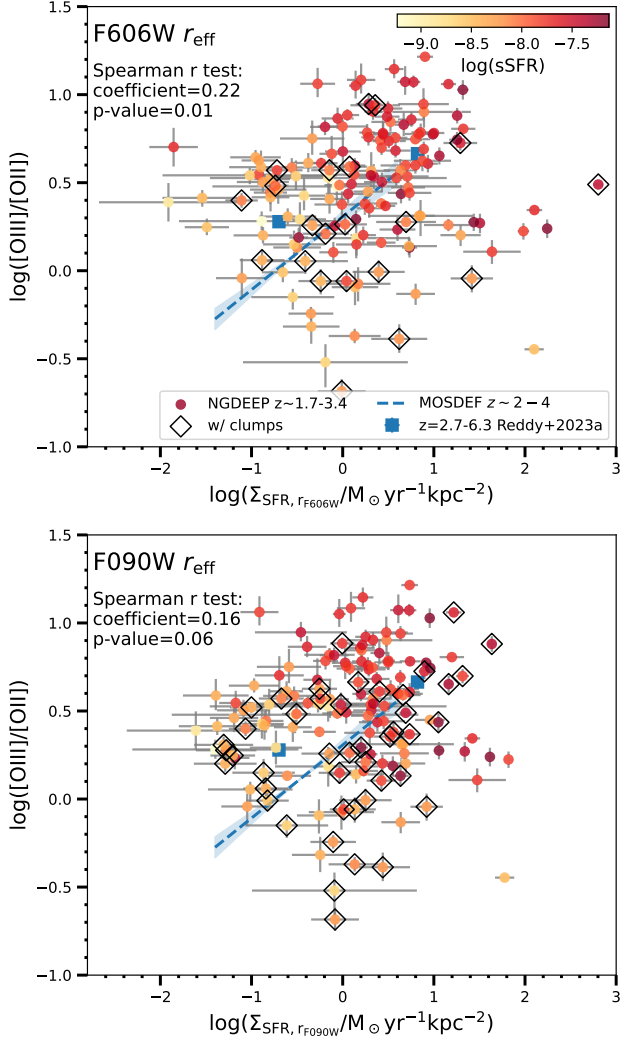


Figure 12. The distribution of the O_{32} ratio and Σ_{SFR} values for the NGDEEP final sample using effective radius measured from the HST F606W (*top*) and JWST F090W images (*bottom*). The data points are color-coded by $s\text{SFR}$. For galaxies identified with more than one component, we use the effective radius of the brightest clump. Such galaxies are marked with open black diamonds. In both panels, the median values of galaxies at $z = 2.7 - 6.3$ from Reddy et al. (2023a) are shown as blue squares, and the fit for MOSDEF galaxies at $z \sim 2 - 4$ (Reddy et al. 2023b) are shown as a blue dotted line. The SFR surface density may contribute to affecting O_{32} , but with a considerable scatter and sensitivity to the bandpass used for size measurements.

As mentioned in the introduction, the hydrogen density is approximately the electron density of an ionized gas. Some studies have suggested that the increased electron densities in high-redshift galaxies could be a major factor contributing to the increase in the ionization parameter (Davies et al. 2021; Reddy et al. 2023b,a). It is important to note that the electron den-

sities from these studies are derived from $[\text{S II}] \lambda\lambda 6716, 6731$ or $[\text{O II}] \lambda\lambda 3726, 3729$, which measures the density in the low-ionization zone. This may differ from the density in higher ionization zones and the average electron density (Berg et al. 2021).

However, we do not have measurements of the electron density. Some studies have found a significant correlation between electron density and SFR *surface density* for galaxies at $z \sim 2$ (Shimakawa et al. 2015; Reddy et al. 2023b). These are related because the n_e of H II regions is governed by the molecular gas density and the balance between stellar feedback and ambient pressure (e.g., Davies et al. 2021), and the molecular gas density is related to the SFR *surface density* via the Kennicutt–Schmidt relation (e.g., Kennicutt et al. 2007; de los Reyes & Kennicutt 2019; Bacchini et al. 2019; Pessa et al. 2021). Here, we investigate whether the SFR surface density is correlated with O_{32} , and whether it affects the ionization parameter.

We derive the SFR surface density as:

$$\Sigma_{\text{SFR}} = \frac{\text{SFR}}{2\pi r_{\text{eff}}^2} [\text{M}_{\odot} \text{ yr}^{-1} \text{ kpc}^{-2}], \quad (9)$$

where r_{eff} is the effective radius of galaxies in units of kpc. For each galaxy, we estimate r_{eff} using two different bandpasses. We used both the HST F606W image and JWST/NIRCAM F090W images, and measured the effective radii with the PYSERSIC code (Pasha & Miller 2023). Because the SFR is derived from SED fitting which mostly relies on far-UV luminosity, we chose the HST F606W image as this corresponds to rest-frame wavelengths of $\simeq 1400\text{--}2250 \text{ \AA}$. However, even though the F090W covers a less ideal set of rest-frame wavelengths $2050\text{--}3200 \text{ \AA}$, it provides better spatial resolution and deeper sensitivity, which is particularly important for measuring the size of small, low-mass galaxies. For the F606W sizes, we run PYSERSIC with a $2'' \times 2''$ cutout centered on the source with the image in a 60 mas scale, a PSF adopted from Finkelstein et al. (2022), and priors from SEP (Bertin & Arnouts 1996; Barbary et al. 2016) with a detection threshold of $5 \times$ the RMS noise and a MINAREA of 5 pixels. We perform the PYSERSIC on F090W with the same setup, but with the image in a 30 mas scale and the PSF from WEBBPSF. For galaxies identified with more than one component in the segmentation, we use the effective radius of the brightest clump.

Figure 12 shows the distribution of O_{32} and Σ_{SFR} based on effective radius measured in F606W and F090W on the top and bottom panels, respectively. We find a significant correlation between O_{32} and Σ_{SFR} when using F606W r_{eff} , with a Spearman correlation

coefficient of 0.22 and a p-value of 0.01. No significant correlation is found between O_{32} and Σ_{SFR} when using F090W r_{eff} with a p-value of 0.06. As a comparison, we show the fitted relation for MOSDEF galaxies at $z \sim 1.9 - 3.7$ derived by Reddy et al. (2023b) and the median values of galaxies at $z = 2.7 - 6.3$ from Reddy et al. (2023a). Our galaxies are scattered around the fitted relation from MOSDEF galaxies with a relatively large scatter of ~ 0.45 dex in both panels. Several potential factors could lead to the difference. Firstly, 18% and 31% of our galaxies show multiple components in the F606W and F090W images, respectively. As mentioned above, for galaxies with multiple detected clumps, we use only the effective radius of the brightest clump, which could underestimate the size of these galaxies and lead to an increase in the Σ_{SFR} . This effect is likely more pronounced in F090W, as more galaxies are spatially resolved into multiple components in this band. In addition, dust could bias our UV size measurements by artificially increasing the apparent size in UV when dust obscuration dominates in the central region of the galaxy (see further discussion in Shen et al. 2023). This effect is likely negligible in low-mass, high-sSFR galaxies in our sample as they have lower dust content and small $E(B - V)$. Another possible reason is that different data is used for size measurements. MOSDEF used the size measured from F160W, where light is dominated by an older stellar population. Meanwhile, the PSF of F160W is larger than F606W and F090W, which could bias the size of compact galaxies. Overall, we argue that the SFR surface density may influence O_{32} , but with a considerable scatter and sensitivity to the bandpass used for size measurements.

Instead of using SFR from SED fitting and UV size, we can directly use $H\alpha$ emission line map to obtain a Σ_{SFR} map. This method is more straightforward and $H\alpha$ is less affected by dust compared with UV. In fact, we see evidence of a positive relation between O_{32} and Σ_{SFR} from the O_{32} ratio maps and $H\alpha$ -derived Σ_{SFR} maps. We will fully explore this in the next paper (Shen et al. in prep).

4.3.3. Density-bounded nebulae

In equation 6, we assumed a radiation-bounded nebula, where all ionizing photons are absorbed and converted to nebular emission. Alternatively, in the case of ‘‘density-bounded’’ nebulae, ionizing photons can escape. This can elevate the O_{32} ratio as the low-ionization region (where most of the [O II] originates) is not fully formed (see Nakajima & Ouchi 2014). Studies of low-redshift galaxies find that the O_{32} ratio correlates with the escape fraction H-ionizing photons, f_{esc} (Chisholm

et al. 2018; Izotov et al. 2018). However, more recent studies suggest that a high O_{32} ratio may be a necessary but not sufficient condition for the large escape fraction (Nakajima et al. 2020; Choustikov et al. 2024). Future direct measurements of the escape fraction for our sample would allow us to test this. This study may be achievable using existing data from UVUDF (Teplitz et al. 2013; Rafelski et al. 2015), which covers rest-frame far-UV continuum at wavelengths $< 912\text{\AA}$. We will explore this in future work.

5. SUMMARY

We study the relation between O_{32} ratios and galaxy properties for 178 SFGs at $1.7 < z < 3.4$ using NIRISS slitless spectroscopy observations from the NGDEEP survey. The O_{32} ratio primarily traces the ionization parameter of the ISM, with a secondary dependence on metallicity. Our sample is selected based on the deep NIRISS spectra, primarily relying on the [O III] emission lines. All galaxies lie above the star-formation main sequence and span a stellar mass range of $10^7 - 10^{10.2} M_{\odot}$. Galaxy properties are estimated with ancillary deep HST and JWST imaging from CANDELS, JADES, and JEMS. Our results are summarized as follows:

- We find significant correlations between the O_{32} ratios and galaxies properties such that the O_{32} ratio increases with decreasing stellar mass, decreasing SFR, increasing sSFR, and increasing EW of $H\alpha$ and $H\beta$.
- We find that the O_{32} ratio is primarily driven by ionization parameters with a secondary dependence on metallicity, consistent with previous observational results and photoionization models. This suggests that the ionization parameter has a similar dependence on galaxy properties as is found for O_{32} .
- Compared to local normal galaxies, galaxies at $z \sim 2 - 3$ have a higher O_{32} ratio at fixed stellar mass and SFR, suggesting higher ionization parameter and/or low metallicity in $z \sim 2 - 3$ galaxies.
- We find that $z \sim 2 - 3$ galaxies have comparable or lower O_{32} to that measured for extreme galaxies at $z \sim 0$ at the fixed stellar mass, SFR, sSFR and $H\alpha$ and $H\beta$ EW, indicating these extreme galaxies at $z \sim 0$ have similar to higher ionization parameter and similar to lower metallicity.
- Our NGDEEP sample spans a wide range of O_{32} and stellar mass, which helps bridge the gap between the local and the $z > 5$ universe. We find

an evolutionary trend in O_{32} and $EW(H\beta)$ from $z \sim 0$ to $z \gtrsim 5$, where higher redshift galaxies show increased O_{32} and EW , with possibly higher O_{32} at fixed EW .

- We investigate the possible physical mechanisms behind the relation between the ionization parameter and recent star formation activity. We find that the O_{32} ratio is significantly correlated with the ionizing production efficiency. Meanwhile, the SFR surface density may contribute to affecting O_{32} , but with a considerable scatter and sensitivity to the bandpass used for size measurements. We argue that both the enhanced recent star formation activity and SFR surface density could be the main contributors to the increase in O_{32} and the ionization parameter.

This paper demonstrates the capability of *JWST*/NIRISS slitless spectroscopy data to measure the nebular emission line for low-mass galaxies $\log(M_*/M_\odot) \sim 10^7 - 10^9$ at $z \sim 2 - 3$. This dataset enables us to constrain star formation, metallicity, ionization parameter, and dust content of entire galaxies, as well as their spatially resolved profiles. With the extended mass range of galaxies, this dataset can bridge the gap between the local and $z > 5$ universe, enabling us to constrain the evolutionary trends of key galaxies and ISM properties.

Facilities: HST (ACS, WFC3), JWST (NIRCAM, NIRISS)

Software: The python packages ASTROPY (Astropy Collaboration et al. 2013, 2018), MATPLOTLIB (Hunter 2007), NUMPY (van der Walt et al. 2011), and SCIPY (Virtanen et al. 2020) were extensively used.

1 We acknowledge the hard work of our colleagues in the
 2 NGDEEP collaboration and everyone involved in the
 3 *JWST* mission. We wish to thank the anonymous referee
 4 for a thorough and constructive report that improved
 5 the quality and clarity of this work. This work
 6 benefited from support from the George P. and Cynthia
 7 Woods Mitchell Institute for Fundamental Physics
 8 and Astronomy at Texas A&M University. CP thanks
 9 Marsha and Ralph Schilling for generous support of this
 10 research. This work is based on observations made with
 11 the NASA/ESA/CSA *JWST*. The data were obtained
 12 from the Mikulski Archive for Space Telescopes at the
 13 Space Telescope Science Institute, which is operated
 14 by the Association of Universities for Research in Astronomy,
 15 Inc., under NASA contract NAS 5-03127 for
 16 *JWST*. These observations are associated with program
 17 #2079. Some/all the *JWST* data presented in this paper
 18 were obtained from the Mikulski Archive for Space Telescopes
 19 (MAST) at the Space Telescope Science Institute.
 20 The specific observations analyzed can be accessed via
 21 Leung, Gene et al. (2023), Williams, Christina et al.
 22 (2023) and Rieke, Marcia et al. (2023). JM is grateful
 23 to the Cosmic Dawn Center for the DAWN Fellowship.

APPENDIX

A. MODEL ESTIMATED STAR FORMATION RATES

CIGALE calculates several different SFRs, including an instantaneous SFR ($\text{SFR}_{\text{instant}}$), and the SFR averaged over 10 Myr ($\text{SFR}_{10\text{Myrs}}$) and 100 Myr ($\text{SFR}_{100\text{Myrs}}$). These SFRs are influenced by the assumed parameterization and the fitted star formation history. To better understand these estimated SFRs, we compare the $\text{H}\alpha$ -derived and $\text{H}\beta$ -derived SFRs ($\text{SFR}_{\text{H}\alpha}$ and $\text{SFR}_{\text{H}\beta}$) with these SED-derived SFRs in Figure A1 for NGDEEP SFGs with $\text{H}\alpha$ and $\text{H}\beta$ emission line flux detected with SNRs > 5 . The $\text{SFR}_{\text{H}\alpha}$ and $\text{SFR}_{\text{H}\beta}$ are calculated from the dust-corrected $\text{H}\alpha$ and $\text{H}\beta$ luminosity using the Kennicutt & Evans (2012) calibration. We assume an intrinsic ratio of $\text{H}\alpha/\text{H}\beta = 2.86$ (based on the Case B assumption for $T = 10^4$ K and $n_e = 10^2 \text{ cm}^{-3}$) when converting the $\text{H}\beta$ luminosity to an SFR. The dust correction applied to $\text{H}\alpha$ and $\text{H}\beta$ is based on $E(B - V)_{\text{star}}$ and SFR derived from SED fitting and follows the (Cardelli et al. 1989) extinction model with $R_V = 3.1$ (as described in Section 2.4 and see Appendix B).

As shown in Figure A1, the instantaneous SFRs and $\text{SFR}_{10\text{Myrs}}$ from CIGALE correlate well with the SFRs derived from the $\text{H}\alpha$ and $\text{H}\beta$ lines. The median difference between the SED-derived SFRs and $\text{SFR}_{\text{H}\alpha}$ are 0.15 and 0.09 dex, for the instantaneous and 10 Myr-averaged SFRs, respectively. However, the $\text{SFR}_{100\text{Myrs}}$ is on average lower than $\text{SFR}_{\text{H}\alpha}$ by -0.17 dex (a factor of order 1.5). We found similar trends when comparing SED-derived SFRs and $\text{SFR}_{\text{H}\beta}$ with differences of 0.10, 0.03, and -0.23 dex for $\text{SFR}_{\text{instant}}$, $\text{SFR}_{10\text{Myrs}}$, and $\text{SFR}_{100\text{Myrs}}$, respectively.

We adopt the LINMIX to fit the relation between SED-derived and $\text{SFR}_{\text{H}\alpha}$ and $\text{SFR}_{\text{H}\beta}$ (if $\text{SFR}_{\text{H}\alpha}$ is not available). The best-fitted lines for $\text{SFR}_{\text{instant}}$ and $\text{SFR}_{10\text{Myrs}}$ align close to the 1-to-1 relation. The 1σ total scatter and intrinsic scatter are similar (~ 0.2 dex and ~ 0.02 - 0.03 dex respectively) in both cases. In contrast, the best-fitted line for $\text{SFR}_{100\text{Myrs}}$ is offset from the 1-to-1 relation and has a larger total and intrinsic scatter (0.32 dex and 0.06 dex, respectively). This is consistent with the fact that the $\text{H}\alpha$ emission is sensitive to ionization from O-type stars with lifetimes of ~ 5 Myr. In the paper, we use $\text{SFR}_{10\text{Myrs}}$ as the SED-derived SFR, which shows the smallest offset compared to $\text{SFR}_{\text{H}\alpha}$ and $\text{SFR}_{\text{H}\beta}$.

B. DUST REDDENING CORRECTION

Ideally, we would use the Balmer decrements (e.g., measured from the $\text{H}\alpha/\text{H}\beta$ line ratios) to estimate nebular dust attenuation. However, because not all galaxies have both $\text{H}\beta$ and $\text{H}\alpha$ covered by NIRISS, we instead rely on the $E(B - V)$ values derived from SED fitting. We consider two methods here: (1) applying a uniform star-to-gas attenuation ratio to convert the SED-derived $E(B - V)_{\text{star}}$ to $E(B - V)_{\text{gas}}$ for nebular emission; and (2) adopting an SFR-dependent star-to-gas attenuation ratio, following the method from Reddy et al. (2015); Sanders et al. (2021). We calibrated and tested these two methods using 65 SFGs from the NGDEEP survey at $1.7 < z < 2.3$ that has detections of both $\text{H}\alpha$ and $\text{H}\beta$ at SNR > 5 . The median redshift of this sample is 2.0.

In the top panel of Figure B2, we show the histogram of the $\text{H}\alpha/\text{H}\beta$ line ratios. There are 48% of the 65 galaxies having $\text{H}\alpha/\text{H}\beta$ ratios lower than the Case B value of 2.86 (based on the Case B assumption for $T = 10^4$ K and $n_e = 10^2 \text{ cm}^{-3}$). The median $\text{H}\alpha/\text{H}\beta$ ratios of our sample is 2.88, with a 16th and 84th percentile range of 2.26 to 4.01. A significant fraction of galaxies with $\text{H}\alpha/\text{H}\beta$ ratios below 2.86 was also reported in Pirzkal et al. (2023) which used NGDEEP epoch 1 data and adopted a different data reduction and extraction method. The low $\text{H}\alpha/\text{H}\beta$ ratios are unlikely to be caused by low SNR or wavelength-dependent flux calibration, as no correlation is observed between these ratios and the SNR of $\text{H}\alpha$ or $\text{H}\beta$ emission lines or the observed wavelength. On the other hand, we find that the $\text{H}\alpha/\text{H}\beta$ ratio is significantly correlated with stellar mass, SFR, and O_{32} as $\text{H}\alpha/\text{H}\beta$ increases with increasing mass, SFR, and with decreasing O_{32} . The correlation between the $\text{H}\alpha/\text{H}\beta$ ratios and SFR is consistent with the finding from (Reddy et al. 2015). Furthermore, (Scarlata et al. 2024) also shows that galaxies with high O_{32} are more likely to have low $\text{H}\alpha/\text{H}\beta$ ratios. These results support that the low $\text{H}\alpha/\text{H}\beta$ ratios are more likely due to physical conditions, such as a different geometry of dust and gas, and higher temperatures in galaxies with high ionization or low metallicity. In such environments, the intrinsic $\text{H}\alpha/\text{H}\beta$ of galaxies could be lower than 2.86. This topic is beyond the primary scope of this paper, so we have not included this analysis in the current work. However, we plan to explore this in greater detail in a future study.

We compared the SED-derived $E(B - V)_{\text{star}}$ and $\text{H}\alpha/\text{H}\beta$ -derived $E(B - V)_{\text{gas}}$ and shown in the bot-

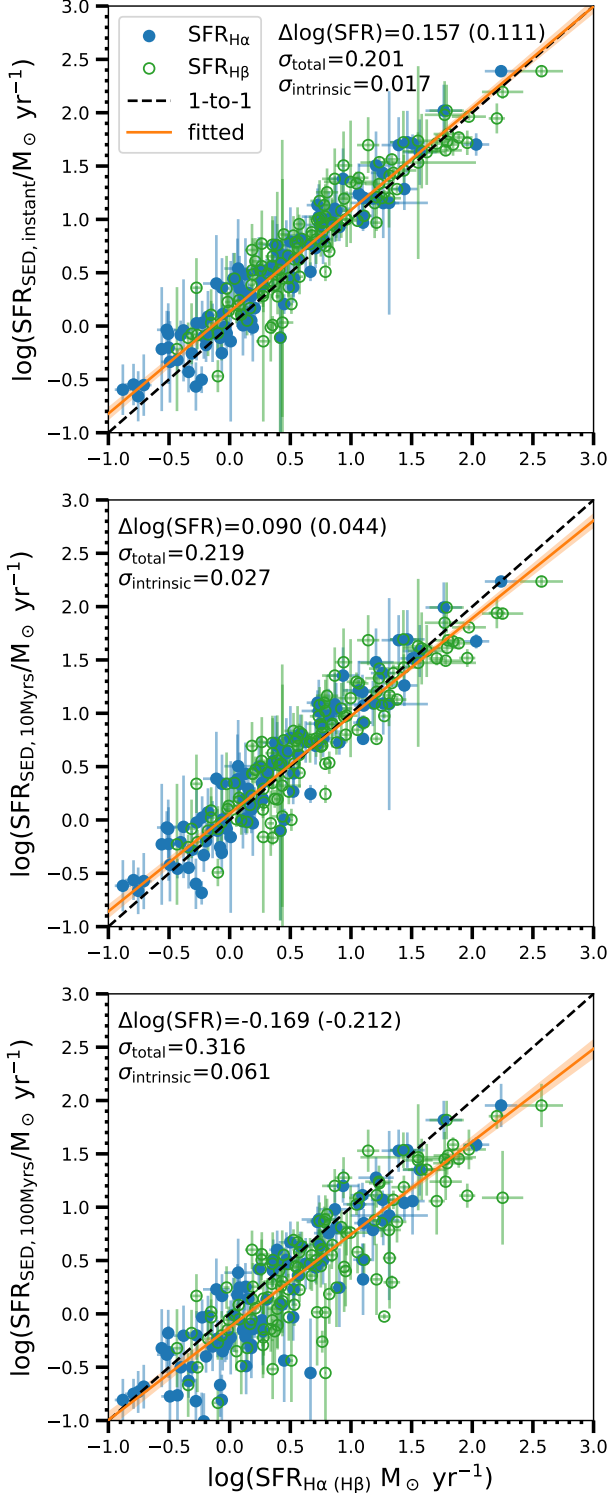


Figure A1. Comparison of the SED-derived instantaneous SFR (*top*), and the SFR averaged over 10 Myr (*middle*) and average over 100 Myr (*bottom*) and H α - and H β -derived SFR for NGDEEP full sample with H α and H β SNR > 5, respectively. In each panel, the solid orange line shows the best-fitted line using LINMIX package (Kelly 2007) using SFR $_{\text{H}\alpha}$ and SFR $_{\text{H}\beta}$ (if SFR $_{\text{H}\alpha}$ is not available). The black dashed line is the 1-to-1 relation. The median offset between SFR $_{\text{SED}}$ and SFR $_{\text{H}\alpha}$ (SFR $_{\text{H}\beta}$) are presented in each panel.

tom panel of Figure B2. For those with H α /H β > 2.86, the SED-derived E(B - V) $_{\text{star}}$ and H α /H β -derived E(B - V) $_{\text{gas}}$ generally follow the E(B - V) $_{\text{star}} = 0.44 \times \text{E}(B - V)_{\text{gas}}$. We measure a median star-to-gas attenuation ratio of 0.67. For those with H α /H β < 2.86, they tend to have low SED-derived E(B - V) $_{\text{star}}$ with the median E(B - V) $_{\text{star}}$ of 0.10, suggesting that the dust attenuation is relatively low in these galaxies. Here, we test on a star-to-gas attenuation ratio of 0.44 and 1. However, if E(B - V) $_{\text{gas}} = 0$ is assumed for galaxies with H α /H β < 2.86, applying this method will overestimate dust in these galaxies.

For the second method, it assumes that the difference between E(B - V) $_{\text{gas}}$ and E(B - V) $_{\text{star}}$ is a function of SFR $_{\text{H}\alpha}$, as found in Reddy et al. (2015) (and references therein). Following Sanders et al. (2021), we quantified relations between E(B - V) $_{\text{gas}} - \text{E}(B - V)_{\text{star}}$ and H α -derived SFR, and between the H α -derived SFR and SED-derived SFR as shown in B3. The best-fit linear relations from LINMIX are:

$$\begin{aligned} \text{E}(B - V)_{\text{gas,calibrated}} - \text{E}(B - V)_{\text{stars}} = \\ (0.332 \pm 0.053) \times \log(\text{SFR}_{\text{H}\alpha}) + (-0.293 \pm 0.045) \end{aligned} \quad (\text{B1})$$

$$\begin{aligned} \log(\text{SFR}_{\text{H}\alpha}) = \\ (0.879 \pm 0.069) \times \log(\text{SFR}_{\text{SED},10\text{Myrs}}) + (0.063 \pm 0.060), \end{aligned} \quad (\text{B2})$$

, where SFR $_{\text{SED},10\text{Myrs}}$ is the SFR average over 10 Myrs derived from CIGALE SED fitting, and SFR $_{\text{H}\alpha}$ is calculated from the dust-corrected H α luminosity using E(B - V) $_{\text{gas}}$ from Balmer decrement and convert to SFR using the Kennicutt & Evans (2012) calibration. The total scatter of E(B - V) $_{\text{gas}} - \text{E}(B - V)_{\text{stars}} - \log(\text{SFR}_{\text{H}\alpha})$ and $\log(\text{SFR}_{\text{H}\alpha}) - \log(\text{SFR}_{\text{SED}})$ relations are 0.24 and 0.30 dex, respectively. The intrinsic scatters are 0.05 and 0.08 dex, respectively.

In the top panels of Figure B4, we compare the calibrated E(B - V) values derived using these two methods to E(B - V) $_{\text{gas}}$ obtained from the Balmer decrement, as a function of stellar mass and SFR. The median offset between the calibrated E(B - V) and E(B - V) $_{\text{gas}}$ is smaller when using an SFR-dependent star-to-gas attenuation ratio, with a median offset of 0.03 dex. This offset does not vary across stellar mass but shows a mild dependence on SFR, with higher calibrated E(B - V) at higher SFRs. In the case of using a uniform star-to-gas attenuation ratio of 0.44 and 1, the median offsets are 0.09 dex and 0.27 dex, respectively, indicating an overestimation of dust correction for these galaxies. This overestimation is particularly pronounced in low stellar masses and low SFRs.

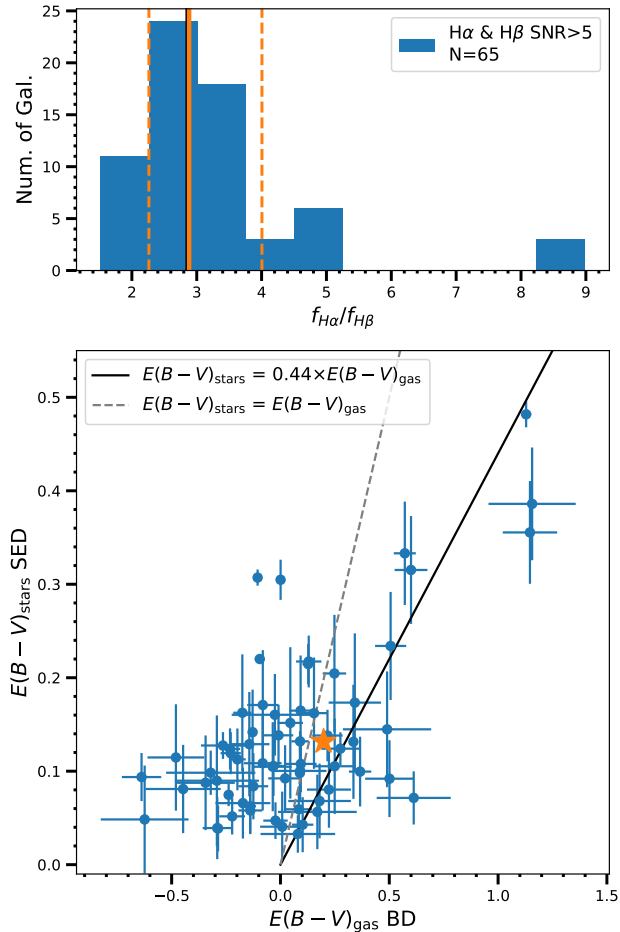


Figure B2. *Top:* Histogram of $H\alpha/H\beta$ emission line ratios for the NGDEEP final sample with $H\alpha$ and $H\beta$ SNR > 5 . The vertical orange solid line indicates the median $H\alpha/H\beta$ ratio, while the dashed lines represent the 16th and 84th percentiles. The vertical black line marks the theoretical minimum value of 2.86 in the absence of dust for Case B recombination. *Bottom:* Comparison of the color excesses derived for the stellar continuum from SED fitting and that for the ionized gas calculated from $H\alpha/H\beta$. The $E(B-V)_{\text{gas}}$ is computed assuming the Cardelli et al. (1989) extinction curve with $R_V = 3.1$. The median stellar-to-gas attenuation ratio for galaxies with $H\alpha/H\beta > 2.86$ is marked by a orange star. The black solid line shows the relation $E(B-V)_{\text{star}} = 0.44 \times E(B-V)_{\text{gas}}$ from Calzetti et al. (2000). The grey dashed line shows the 1-to-1 relation between $E(B-V)_{\text{star}}$ and $E(B-V)_{\text{gas}}$.

As we focus on the relations between the O_{32} ratio and various galaxy properties, we compare the offset between O_{32} using the calibrated $E(B-V)$ values derived using these two methods to those using $E(B-V)_{\text{gas}}$ from the Balmer decrement. We adopt the same Cardelli et al. (1989) extinction model with $R_V = 3.1$. For galaxies with $E(B-V) < 0$, no dust correction is applied. The O_{32} offsets are shown as a function of stellar mass in the bottom panels of Figure B4. The median offset is 0 when the SFR-dependent attenuation ratio, and the median offset increases to -0.03 and -0.09 when using a uniform star-to-gas attenuation ratio of 1 and 0.04, respectively. Similar to the $E(B-V)$ comparison, the offsets from method 2 do not vary across stellar mass but show a mild dependence on SFR, suggesting that O_{32} might be underestimated at high SFR by ~ 0.04 . The offsets from method 1 using a ratio of 1 show dependence on both stellar mass and SFR. This comparison shows that applying different reddening corrections could impact the O_{32} ratio up to ~ 0.1 dex. The effect may depend on stellar mass and SFR, potentially influencing the derived relations.

In this paper, for the dust correction of emission lines (i.e., $[O\text{ III}] H\beta$, $[O\text{ II}] H\alpha$), we adopt the second method using equation 1 and 2, which provides consistent $E(B-V)$ and O_{32} compared to those using the Balmer decrement and consistent SFR from dust-corrected $H\alpha$ and $H\beta$ (see Figure A1). We note that while the significances and slopes of the O_{32} -galaxy property relations presented in this paper remain unchanged if a uniform star-to-gas attenuation ratio of 0.44 or 1 (first method) is adopted, the intercept of these relations would be systematically shifted lower by ~ 0.09 dex or ~ 0.03 dex.

REFERENCES

- Astropy Collaboration, Robitaille, T. P., Tollerud, E. J., et al. 2013, *A&A*, 558, A33, doi: [10.1051/0004-6361/201322068](https://doi.org/10.1051/0004-6361/201322068)
- Astropy Collaboration, Price-Whelan, A. M., Sipőcz, B. M., et al. 2018, *AJ*, 156, 123, doi: [10.3847/1538-3881/aabc4f](https://doi.org/10.3847/1538-3881/aabc4f)
- Bacchini, C., Fraternali, F., Iorio, G., & Pezzulli, G. 2019, *A&A*, 622, A64, doi: [10.1051/0004-6361/201834382](https://doi.org/10.1051/0004-6361/201834382)
- Bagley, M. B., Finkelstein, S. L., Koekemoer, A. M., et al. 2022, arXiv e-prints, arXiv:2211.02495. <https://arxiv.org/abs/2211.02495>

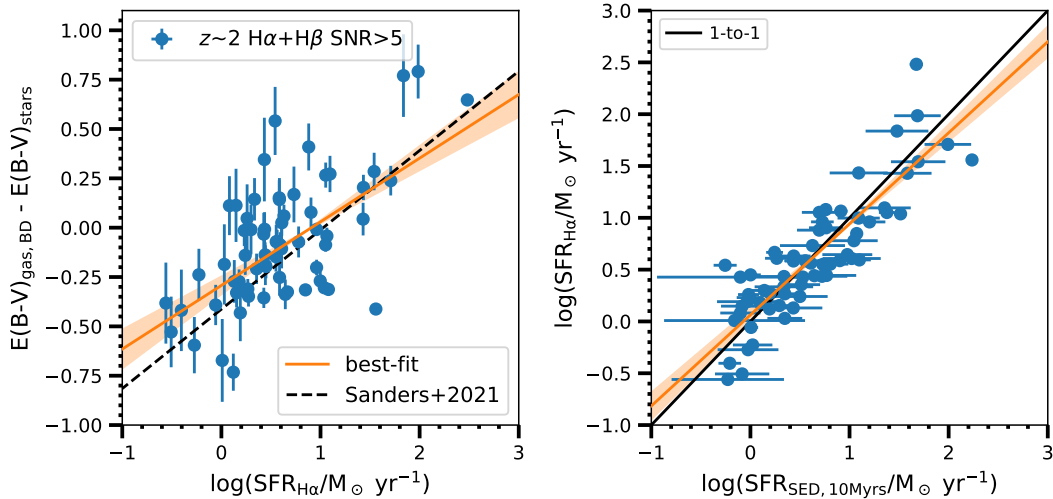


Figure B3. *Left:* The difference between nebular reddening $E(B - V)_{\text{gas, BD}}$ derived using the Balmer decrement (BD) and stellar reddening $E(B - V)_{\text{star}}$ from SED fitting as a function of $\text{SFR}_{\text{H}\alpha}$ for SFGs at $z \sim 2$ with detections of both $\text{H}\alpha$ and $\text{H}\beta$ $\text{SNR} > 5$. The orange solid line shows the best fit, with the shaded region indicating the 1σ uncertainties. The dashed black line shows the relation from Sanders et al. (2021). *Right:* $\text{SFR}_{\text{H}\alpha}$ vs. $\text{SFR}_{\text{SED}, 10\text{Myrs}}$. The solid black line shows the 1-to-1 relation.

Baldwin, J. A., Phillips, M. M., & Terlevich, R. 1981, *PASP*, 93, 5, doi: [10.1086/130766](https://doi.org/10.1086/130766)

Barbary, K., Boone, K., McCully, C., et al. 2016, *kbarbary/sep*: v1.0.0, v1.0.0, Zenodo, doi: [10.5281/zenodo.159035](https://doi.org/10.5281/zenodo.159035)

Berg, D. A., Chisholm, J., Erb, D. K., et al. 2021, *ApJ*, 922, 170, doi: [10.3847/1538-4357/ac141b](https://doi.org/10.3847/1538-4357/ac141b)

Berg, D. A., James, B. L., King, T., et al. 2022, *ApJS*, 261, 31, doi: [10.3847/1538-4365/ac6c03](https://doi.org/10.3847/1538-4365/ac6c03)

Bertin, E., & Arnouts, S. 1996, *A&AS*, 117, 393, doi: [10.1051/aas:1996164](https://doi.org/10.1051/aas:1996164)

Bian, F., Kewley, L. J., Dopita, M. A., & Juneau, S. 2016, *ApJ*, 822, 62, doi: [10.3847/0004-637X/822/2/62](https://doi.org/10.3847/0004-637X/822/2/62)

Blanc, G. A., Kewley, L., Vogt, F. P. A., & Dopita, M. A. 2015, *ApJ*, 798, 99, doi: [10.1088/0004-637X/798/2/99](https://doi.org/10.1088/0004-637X/798/2/99)

Boquien, M., Burgarella, D., Roehlly, Y., et al. 2019, *A&A*, 622, A103, doi: [10.1051/0004-6361/201834156](https://doi.org/10.1051/0004-6361/201834156)

Brammer, G., & Matharu, J. 2021, *gbrammer/grizli*: Release 2021, 1.3.2, Zenodo, doi: [10.5281/zenodo.5012699](https://doi.org/10.5281/zenodo.5012699)

Brinchmann, J., Charlot, S., White, S. D. M., et al. 2004, *MNRAS*, 351, 1151, doi: [10.1111/j.1365-2966.2004.07881.x](https://doi.org/10.1111/j.1365-2966.2004.07881.x)

Bruzual, G., & Charlot, S. 2003, *MNRAS*, 344, 1000, doi: [10.1046/j.1365-8711.2003.06897.x](https://doi.org/10.1046/j.1365-8711.2003.06897.x)

Calzetti, D., Armus, L., Bohlin, R. C., et al. 2000, *ApJ*, 533, 682, doi: [10.1086/308692](https://doi.org/10.1086/308692)

Cardelli, J. A., Clayton, G. C., & Mathis, J. S. 1989, *ApJ*, 345, 245, doi: [10.1086/167900](https://doi.org/10.1086/167900)

Chabrier, G. 2003, *PASP*, 115, 763, doi: [10.1086/376392](https://doi.org/10.1086/376392)

Chisholm, J., Gazagnes, S., Schaerer, D., et al. 2018, *A&A*, 616, A30, doi: [10.1051/0004-6361/201832758](https://doi.org/10.1051/0004-6361/201832758)

Choustikov, N., Katz, H., Saxena, A., et al. 2024, *MNRAS*, 529, 3751, doi: [10.1093/mnras/stae776](https://doi.org/10.1093/mnras/stae776)

Conroy, C., & Gunn, J. E. 2010, *FSPS: Flexible Stellar Population Synthesis*, Astrophysics Source Code Library, record ascl:1010.043

Cullen, F., Cirasuolo, M., McLure, R. J., Dunlop, J. S., & Bowler, R. A. A. 2014, *MNRAS*, 440, 2300, doi: [10.1093/mnras/stu443](https://doi.org/10.1093/mnras/stu443)

Curti, M., Mannucci, F., Cresci, G., & Maiolino, R. 2020, *MNRAS*, 491, 944, doi: [10.1093/mnras/stz2910](https://doi.org/10.1093/mnras/stz2910)

Curti, M., Maiolino, R., Curtis-Lake, E., et al. 2024, *A&A*, 684, A75, doi: [10.1051/0004-6361/202346698](https://doi.org/10.1051/0004-6361/202346698)

Davies, R. L., Förster Schreiber, N. M., Genzel, R., et al. 2021, *ApJ*, 909, 78, doi: [10.3847/1538-4357/abd551](https://doi.org/10.3847/1538-4357/abd551)

de los Reyes, M. A. C., & Kennicutt, Robert C., J. 2019, *ApJ*, 872, 16, doi: [10.3847/1538-4357/aafa82](https://doi.org/10.3847/1538-4357/aafa82)

Dickinson, M., Amorin, R., Arrabal Haro, P., et al. 2024, *The CANDELS-Area Prism Epoch of Reionization Survey (CAPERS)*, JWST Proposal. Cycle 3, ID. #6368

Dopita, M. A., & Sutherland, R. S. 1996, *ApJS*, 102, 161, doi: [10.1086/192255](https://doi.org/10.1086/192255)

—. 2003, *Astrophysics of the diffuse universe*, doi: [10.1007/978-3-662-05866-4](https://doi.org/10.1007/978-3-662-05866-4)

Eisenstein, D. J., Willott, C., Albers, S., et al. 2023, *arXiv e-prints*, arXiv:2306.02465, doi: [10.48550/arXiv.2306.02465](https://doi.org/10.48550/arXiv.2306.02465)

Emami, N., Siana, B., Alavi, A., et al. 2020, *ApJ*, 895, 116, doi: [10.3847/1538-4357/ab8f97](https://doi.org/10.3847/1538-4357/ab8f97)

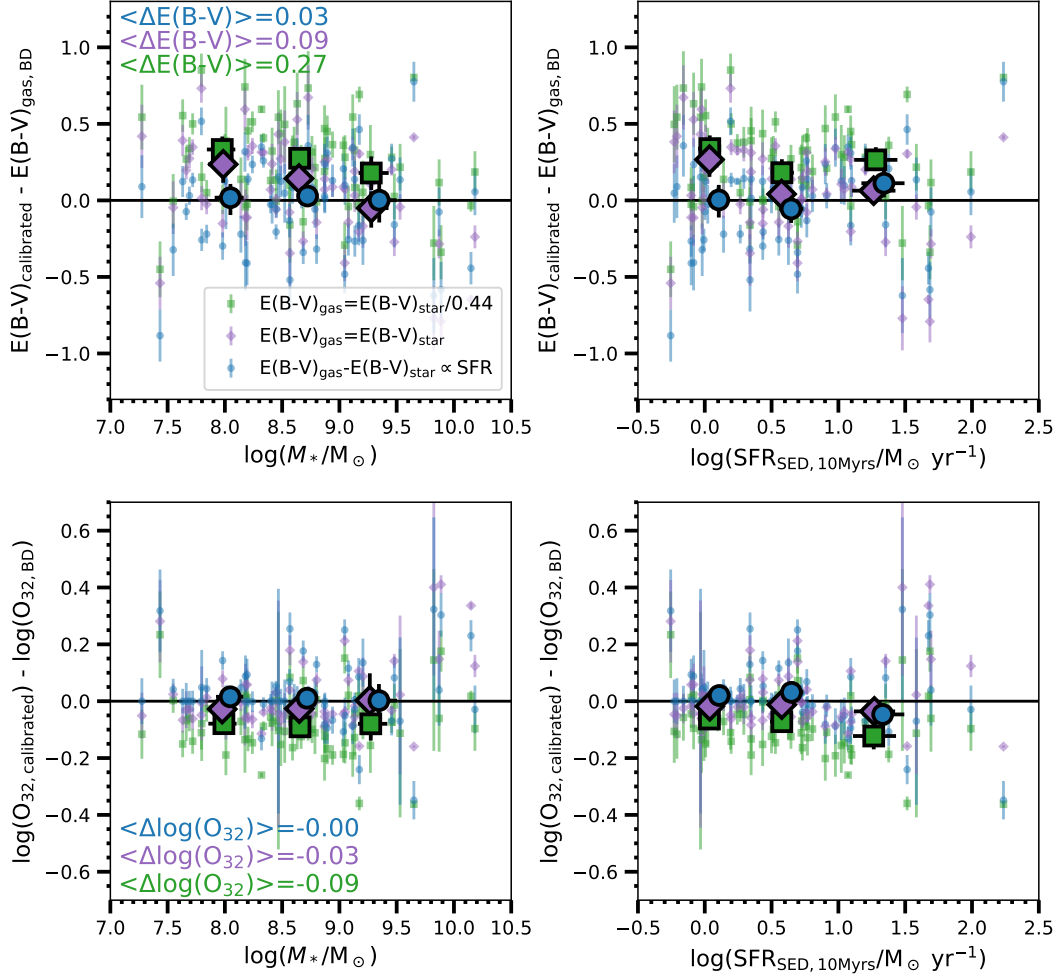


Figure B4. *Tops:* Comparison of calibrated $E(B-V)$ using a uniform star-to-gas attenuation ratio of 0.44 (green squares) or 1 (purple diamonds) or an SFR-dependent star-to-gas attenuation ratio (blue dots) to $E(B-V)_{\text{gas}}$ from the Balmer decrement as a function of stellar mass (left) and SFR (right). *Bottoms:* Comparison of O_{32} using calibrated $E(B-V)$ based on $E(B-V)_{\text{star}}$ and $E(B-V)_{\text{gas}}$ from the Balmer decrement as a function of stellar mass and SFR. The median values are shown as larger markers. The median values using an SFR-dependent star-to-gas attenuation ratio (blue circles) are shifted to the right for clarity.

Emami, N., Siana, B., Weisz, D. R., et al. 2019, *ApJ*, 881, 71, doi: [10.3847/1538-4357/ab211a](https://doi.org/10.3847/1538-4357/ab211a)
 Endsley, R., Stark, D. P., Chevillard, J., & Charlot, S. 2021, *MNRAS*, 500, 5229, doi: [10.1093/mnras/staa3370](https://doi.org/10.1093/mnras/staa3370)
 Erb, D. K., Steidel, C. C., Shapley, A. E., et al. 2006, *ApJ*, 647, 128, doi: [10.1086/505341](https://doi.org/10.1086/505341)
 Estrada-Carpenter, V., Papovich, C., Momcheva, I., et al. 2019, *ApJ*, 870, 133, doi: [10.3847/1538-4357/aaf22e](https://doi.org/10.3847/1538-4357/aaf22e)
 Faisst, A. L., Capak, P. L., Emami, N., Tacchella, S., & Larson, K. L. 2019, *ApJ*, 884, 133, doi: [10.3847/1538-4357/ab425b](https://doi.org/10.3847/1538-4357/ab425b)
 Faisst, A. L., Masters, D., Wang, Y., et al. 2018, *ApJ*, 855, 132, doi: [10.3847/1538-4357/aab1fc](https://doi.org/10.3847/1538-4357/aab1fc)
 Finkelstein, S. L., Bagley, M., Song, M., et al. 2022, *ApJ*, 928, 52, doi: [10.3847/1538-4357/ac3aed](https://doi.org/10.3847/1538-4357/ac3aed)

Finkelstein, S. L., Leung, G. C. K., Bagley, M. B., et al. 2024, *ApJL*, 969, L2, doi: [10.3847/2041-8213/ad4495](https://doi.org/10.3847/2041-8213/ad4495)
 Fukugita, M., Ichikawa, T., Gunn, J. E., et al. 1996, *AJ*, 111, 1748, doi: [10.1086/117915](https://doi.org/10.1086/117915)
 Grogin, N. A., Kocevski, D. D., Faber, S. M., et al. 2011, *ApJS*, 197, 35, doi: [10.1088/0067-0049/197/2/35](https://doi.org/10.1088/0067-0049/197/2/35)
 Guo, Y., Rafelski, M., Faber, S. M., et al. 2016, *ApJ*, 833, 37, doi: [10.3847/1538-4357/833/1/37](https://doi.org/10.3847/1538-4357/833/1/37)
 Hu, W., Papovich, C., Dickinson, M., et al. 2024, *ApJ*, 971, 21, doi: [10.3847/1538-4357/ad5015](https://doi.org/10.3847/1538-4357/ad5015)
 Hunter, J. D. 2007, *Computing in Science and Engineering*, 9, 90, doi: [10.1109/MCSE.2007.55](https://doi.org/10.1109/MCSE.2007.55)
 Inoue, A. K. 2011, *MNRAS*, 415, 2920, doi: [10.1111/j.1365-2966.2011.18906.x](https://doi.org/10.1111/j.1365-2966.2011.18906.x)

- Izotov, Y. I., Worseck, G., Schaerer, D., et al. 2021, *MNRAS*, 503, 1734, doi: [10.1093/mnras/stab612](https://doi.org/10.1093/mnras/stab612)
- . 2018, *MNRAS*, 478, 4851, doi: [10.1093/mnras/sty1378](https://doi.org/10.1093/mnras/sty1378)
- Jones, T., Martin, C., & Cooper, M. C. 2015, *ApJ*, 813, 126, doi: [10.1088/0004-637X/813/2/126](https://doi.org/10.1088/0004-637X/813/2/126)
- Jung, I., Finkelstein, S. L., Arrabal Haro, P., et al. 2024, *ApJ*, 967, 73, doi: [10.3847/1538-4357/ad3913](https://doi.org/10.3847/1538-4357/ad3913)
- Kaasinen, M., Kewley, L., Bian, F., et al. 2018, *MNRAS*, 477, 5568, doi: [10.1093/mnras/sty1012](https://doi.org/10.1093/mnras/sty1012)
- Kashino, D., Silverman, J. D., Sanders, D., et al. 2019, *ApJS*, 241, 10, doi: [10.3847/1538-4365/ab06c4](https://doi.org/10.3847/1538-4365/ab06c4)
- Kauffmann, G., Heckman, T. M., Tremonti, C., et al. 2003, *MNRAS*, 346, 1055, doi: [10.1111/j.1365-2966.2003.07154.x](https://doi.org/10.1111/j.1365-2966.2003.07154.x)
- Kelly, B. C. 2007, *ApJ*, 665, 1489, doi: [10.1086/519947](https://doi.org/10.1086/519947)
- Kennicutt, Robert C., J., Calzetti, D., Walter, F., et al. 2007, *ApJ*, 671, 333, doi: [10.1086/522300](https://doi.org/10.1086/522300)
- Kennicutt, R. C., & Evans, N. J. 2012, *ARA&A*, 50, 531, doi: [10.1146/annurev-astro-081811-125610](https://doi.org/10.1146/annurev-astro-081811-125610)
- Kewley, L. J., & Dopita, M. A. 2002, *ApJS*, 142, 35, doi: [10.1086/341326](https://doi.org/10.1086/341326)
- Kewley, L. J., Dopita, M. A., Leitherer, C., et al. 2013, *ApJ*, 774, 100, doi: [10.1088/0004-637X/774/2/100](https://doi.org/10.1088/0004-637X/774/2/100)
- Kewley, L. J., Nicholls, D. C., Sutherland, R., et al. 2019a, *ApJ*, 880, 16, doi: [10.3847/1538-4357/ab16ed](https://doi.org/10.3847/1538-4357/ab16ed)
- Kewley, L. J., Nicholls, D. C., & Sutherland, R. S. 2019b, *ARA&A*, 57, 511, doi: [10.1146/annurev-astro-081817-051832](https://doi.org/10.1146/annurev-astro-081817-051832)
- Kewley, L. J., Zahid, H. J., Geller, M. J., et al. 2015, *ApJL*, 812, L20, doi: [10.1088/2041-8205/812/2/L20](https://doi.org/10.1088/2041-8205/812/2/L20)
- Koekemoer, A. M., Faber, S. M., Ferguson, H. C., et al. 2011, *ApJS*, 197, 36, doi: [10.1088/0067-0049/197/2/36](https://doi.org/10.1088/0067-0049/197/2/36)
- Kriek, M., Shapley, A. E., Reddy, N. A., et al. 2015, *ApJS*, 218, 15, doi: [10.1088/0067-0049/218/2/15](https://doi.org/10.1088/0067-0049/218/2/15)
- Kroupa, P. 2001, *MNRAS*, 322, 231, doi: [10.1046/j.1365-8711.2001.04022.x](https://doi.org/10.1046/j.1365-8711.2001.04022.x)
- Leitherer, C., & Heckman, T. M. 1995, *ApJS*, 96, 9, doi: [10.1086/192112](https://doi.org/10.1086/192112)
- Leung, Gene, Finkelstein, Steven, Papovich, Casey, & Pirzkal, Norbert. 2023, NGDEEP Epoch 1 NIRC*am* imaging data, STScI/MAST, doi: [10.17909/3S7H-8K54](https://doi.org/10.17909/3S7H-8K54)
- Lyu, J., Alberts, S., Rieke, G. H., & Rujopakarn, W. 2022, *ApJ*, 941, 191, doi: [10.3847/1538-4357/ac9e5d](https://doi.org/10.3847/1538-4357/ac9e5d)
- Madau, P., & Dickinson, M. 2014, *ARA&A*, 52, 415, doi: [10.1146/annurev-astro-081811-125615](https://doi.org/10.1146/annurev-astro-081811-125615)
- Maiolino, R., Nagao, T., Grazian, A., et al. 2008, *A&A*, 488, 463, doi: [10.1051/0004-6361:200809678](https://doi.org/10.1051/0004-6361:200809678)
- Matharu, J., Muzzin, A., Brammer, G. B., et al. 2021, *ApJ*, 923, 222, doi: [10.3847/1538-4357/ac26c3](https://doi.org/10.3847/1538-4357/ac26c3)
- Matharu, J., Muzzin, A., Sarrouh, G. T. E., et al. 2023, *ApJL*, 949, L11, doi: [10.3847/2041-8213/acd1db](https://doi.org/10.3847/2041-8213/acd1db)
- Mingozzi, M., Belfiore, F., Cresci, G., et al. 2020, *A&A*, 636, A42, doi: [10.1051/0004-6361/201937203](https://doi.org/10.1051/0004-6361/201937203)
- Nakajima, K., Ellis, R. S., Robertson, B. E., Tang, M., & Stark, D. P. 2020, *ApJ*, 889, 161, doi: [10.3847/1538-4357/ab6604](https://doi.org/10.3847/1538-4357/ab6604)
- Nakajima, K., & Ouchi, M. 2014, *MNRAS*, 442, 900, doi: [10.1093/mnras/stu902](https://doi.org/10.1093/mnras/stu902)
- Noiro, G., Desprez, G., Asada, Y., et al. 2023, *MNRAS*, 525, 1867, doi: [10.1093/mnras/stad1019](https://doi.org/10.1093/mnras/stad1019)
- Oke, J. B., & Gunn, J. E. 1983, *ApJ*, 266, 713, doi: [10.1086/160817](https://doi.org/10.1086/160817)
- Osterbrock, D. E., & Ferland, G. J. 2006, *Astrophysics of gaseous nebulae and active galactic nuclei*
- Papovich, C., Simons, R. C., Estrada-Carpenter, V., et al. 2022, *ApJ*, 937, 22, doi: [10.3847/1538-4357/ac8058](https://doi.org/10.3847/1538-4357/ac8058)
- Pasha, I., & Miller, T. B. 2023, *Journal of Open Source Software*, 8, 5703, doi: [10.21105/joss.05703](https://doi.org/10.21105/joss.05703)
- Pessa, I., Schinnerer, E., Belfiore, F., et al. 2021, *A&A*, 650, A134, doi: [10.1051/0004-6361/202140733](https://doi.org/10.1051/0004-6361/202140733)
- Pirzkal, N., Rothberg, B., Papovich, C., et al. 2023, *arXiv e-prints*, arXiv:2312.09972, doi: [10.48550/arXiv.2312.09972](https://doi.org/10.48550/arXiv.2312.09972)
- Planck Collaboration, Ade, P. A. R., Aghanim, N., et al. 2016, *A&A*, 594, A13, doi: [10.1051/0004-6361/201525830](https://doi.org/10.1051/0004-6361/201525830)
- Prieto-Lyon, G., Strait, V., Mason, C. A., et al. 2023, *A&A*, 672, A186, doi: [10.1051/0004-6361/202245532](https://doi.org/10.1051/0004-6361/202245532)
- Rafelski, M., Teplitz, H. I., Gardner, J. P., et al. 2015, *AJ*, 150, 31, doi: [10.1088/0004-6256/150/1/31](https://doi.org/10.1088/0004-6256/150/1/31)
- Reddy, N. A., Topping, M. W., Sanders, R. L., Shapley, A. E., & Brammer, G. 2023a, *ApJ*, 952, 167, doi: [10.3847/1538-4357/acd754](https://doi.org/10.3847/1538-4357/acd754)
- Reddy, N. A., Kriek, M., Shapley, A. E., et al. 2015, *ApJ*, 806, 259, doi: [10.1088/0004-637X/806/2/259](https://doi.org/10.1088/0004-637X/806/2/259)
- Reddy, N. A., Shapley, A. E., Sanders, R. L., et al. 2018, *ApJ*, 869, 92, doi: [10.3847/1538-4357/aaed1e](https://doi.org/10.3847/1538-4357/aaed1e)
- Reddy, N. A., Sanders, R. L., Shapley, A. E., et al. 2023b, *ApJ*, 951, 56, doi: [10.3847/1538-4357/acd0b1](https://doi.org/10.3847/1538-4357/acd0b1)
- Rieke, M., & the JADES Collaboration. 2023, *arXiv e-prints*, arXiv:2306.02466, doi: [10.48550/arXiv.2306.02466](https://doi.org/10.48550/arXiv.2306.02466)
- Rieke, Marcia, Robertson, Brant, Tacchella, Sandro, et al. 2023, Data from the JWST Advanced Deep Extragalactic Survey (JADES), STScI/MAST, doi: [10.17909/8TDJ-8N28](https://doi.org/10.17909/8TDJ-8N28)
- Sanders, R. L., Shapley, A. E., Topping, M. W., Reddy, N. A., & Brammer, G. B. 2024, *ApJ*, 962, 24, doi: [10.3847/1538-4357/ad15fc](https://doi.org/10.3847/1538-4357/ad15fc)

- Sanders, R. L., Shapley, A. E., Kriek, M., et al. 2016, *ApJ*, 816, 23, doi: [10.3847/0004-637X/816/1/23](https://doi.org/10.3847/0004-637X/816/1/23)
- . 2018, *ApJ*, 858, 99, doi: [10.3847/1538-4357/aabcbcd](https://doi.org/10.3847/1538-4357/aabcbcd)
- Sanders, R. L., Shapley, A. E., Reddy, N. A., et al. 2020, *MNRAS*, 491, 1427, doi: [10.1093/mnras/stz3032](https://doi.org/10.1093/mnras/stz3032)
- Sanders, R. L., Shapley, A. E., Jones, T., et al. 2021, *ApJ*, 914, 19, doi: [10.3847/1538-4357/abf4c1](https://doi.org/10.3847/1538-4357/abf4c1)
- Scarlata, C., Hayes, M., Panagia, N., et al. 2024, arXiv e-prints, arXiv:2404.09015, doi: [10.48550/arXiv.2404.09015](https://doi.org/10.48550/arXiv.2404.09015)
- Shen, L., Papovich, C., Yang, G., et al. 2023, *ApJ*, 950, 7, doi: [10.3847/1538-4357/acc944](https://doi.org/10.3847/1538-4357/acc944)
- Shen, L., Papovich, C., Matharu, J., et al. 2024, *ApJL*, 963, L49, doi: [10.3847/2041-8213/ad28bd](https://doi.org/10.3847/2041-8213/ad28bd)
- Shimakawa, R., Kodama, T., Steidel, C. C., et al. 2015, *MNRAS*, 451, 1284, doi: [10.1093/mnras/stv915](https://doi.org/10.1093/mnras/stv915)
- Simons, R. C., Papovich, C., Momcheva, I., et al. 2021, *ApJ*, 923, 203, doi: [10.3847/1538-4357/ac28f4](https://doi.org/10.3847/1538-4357/ac28f4)
- Simons, R. C., Papovich, C., Momcheva, I. G., et al. 2023, *ApJS*, 266, 13, doi: [10.3847/1538-4365/acc517](https://doi.org/10.3847/1538-4365/acc517)
- Somerville, R. S., & Davé, R. 2015, *ARA&A*, 53, 51, doi: [10.1146/annurev-astro-082812-140951](https://doi.org/10.1146/annurev-astro-082812-140951)
- Steidel, C. C., Rudie, G. C., Strom, A. L., et al. 2014, *ApJ*, 795, 165, doi: [10.1088/0004-637X/795/2/165](https://doi.org/10.1088/0004-637X/795/2/165)
- Strom, A. L., Steidel, C. C., Rudie, G. C., Trainor, R. F., & Pettini, M. 2018, *ApJ*, 868, 117, doi: [10.3847/1538-4357/aae1a5](https://doi.org/10.3847/1538-4357/aae1a5)
- Strom, A. L., Steidel, C. C., Rudie, G. C., et al. 2017, *ApJ*, 836, 164, doi: [10.3847/1538-4357/836/2/164](https://doi.org/10.3847/1538-4357/836/2/164)
- Sutherland, R. S., & Dopita, M. A. 1993, *ApJS*, 88, 253, doi: [10.1086/191823](https://doi.org/10.1086/191823)
- Tang, M., Stark, D. P., Chevallard, J., & Charlot, S. 2019, *MNRAS*, 489, 2572, doi: [10.1093/mnras/stz2236](https://doi.org/10.1093/mnras/stz2236)
- Teplitz, H. I., Rafelski, M., Kurczynski, P., et al. 2013, *AJ*, 146, 159, doi: [10.1088/0004-6256/146/6/159](https://doi.org/10.1088/0004-6256/146/6/159)
- Tomczak, A. R., Quadri, R. F., Tran, K.-V. H., et al. 2014, *ApJ*, 783, 85, doi: [10.1088/0004-637X/783/2/85](https://doi.org/10.1088/0004-637X/783/2/85)
- . 2016, *ApJ*, 817, 118, doi: [10.3847/0004-637X/817/2/118](https://doi.org/10.3847/0004-637X/817/2/118)
- Tremonti, C. A., Heckman, T. M., Kauffmann, G., et al. 2004, *ApJ*, 613, 898, doi: [10.1086/423264](https://doi.org/10.1086/423264)
- van der Walt, S., Colbert, S. C., & Varoquaux, G. 2011, *Computing in Science and Engineering*, 13, 22, doi: [10.1109/MCSE.2011.37](https://doi.org/10.1109/MCSE.2011.37)
- Virtanen, P., Gommers, R., Oliphant, T. E., et al. 2020, *Nature Methods*, 17, 261, doi: [10.1038/s41592-019-0686-2](https://doi.org/10.1038/s41592-019-0686-2)
- Wang, X., Jones, T., Vulcani, B., et al. 2022, *ApJL*, 938, L16, doi: [10.3847/2041-8213/ac959e](https://doi.org/10.3847/2041-8213/ac959e)
- Whitaker, K. E., Labbé, I., van Dokkum, P. G., et al. 2011, *ApJ*, 735, 86, doi: [10.1088/0004-637X/735/2/86](https://doi.org/10.1088/0004-637X/735/2/86)
- Whitaker, K. E., Franx, M., Leja, J., et al. 2014, *ApJ*, 795, 104, doi: [10.1088/0004-637X/795/2/104](https://doi.org/10.1088/0004-637X/795/2/104)
- Williams, C. C., Tacchella, S., Maseda, M. V., et al. 2023, arXiv e-prints, arXiv:2301.09780, doi: [10.48550/arXiv.2301.09780](https://doi.org/10.48550/arXiv.2301.09780)
- Williams, Christina, Tacchella, Sandro, & Maseda, Michael. 2023, Data from the JWST Extragalactic Medium-band Survey (JEMS), STScI/MAST, doi: [10.17909/FSC4-DT61](https://doi.org/10.17909/FSC4-DT61)
- Yang, G., Boquien, M., Buat, V., et al. 2020, *MNRAS*, 491, 740, doi: [10.1093/mnras/stz3001](https://doi.org/10.1093/mnras/stz3001)
- Yang, H., Malhotra, S., Rhoads, J. E., & Wang, J. 2017a, *ApJ*, 847, 38, doi: [10.3847/1538-4357/aa8809](https://doi.org/10.3847/1538-4357/aa8809)
- Yang, H., Malhotra, S., Gronke, M., et al. 2017b, *ApJ*, 844, 171, doi: [10.3847/1538-4357/aa7d4d](https://doi.org/10.3847/1538-4357/aa7d4d)
- Yates, R. M., Schady, P., Chen, T. W., Schweyer, T., & Wiseman, P. 2020, *A&A*, 634, A107, doi: [10.1051/0004-6361/201936506](https://doi.org/10.1051/0004-6361/201936506)
- Zahid, H. J., Dima, G. I., Kudritzki, R.-P., et al. 2014, *ApJ*, 791, 130, doi: [10.1088/0004-637X/791/2/130](https://doi.org/10.1088/0004-637X/791/2/130)
- Zahid, H. J., Kewley, L. J., & Bresolin, F. 2011, *ApJ*, 730, 137, doi: [10.1088/0004-637X/730/2/137](https://doi.org/10.1088/0004-637X/730/2/137)